



# SDSS-IV eBOSS Spectroscopy of X-Ray and *WISE* AGNs in Stripe 82X: Overview of the Demographics of X-Ray- and Mid-infrared-selected Active Galactic Nuclei

Stephanie M. LaMassa<sup>1</sup> , Antonis Georgakakis<sup>2</sup>, M. Vivek<sup>3,4</sup>, Mara Salvato<sup>5</sup> , Tonima Tasnim Ananna<sup>6,7</sup> , C. Meg Urry<sup>6,7</sup> , Chelsea MacLeod<sup>8</sup>, and Nicholas Ross<sup>9</sup>

<sup>1</sup> Space Telescope Science Institute, 3700 San Martin Drive, Baltimore, MD 21210, USA

<sup>2</sup> National Observatory of Athens, Vas. Pavlou & I. Metaxa, 15236 Penteli, Greece

<sup>3</sup> Department of Astronomy and Astrophysics, The Pennsylvania State University, 525 Davey Lab, University Park, PA 16802, USA

<sup>4</sup> Department of Physics & Astronomy, University of Utah, Salt Lake City, UT 84112, USA

<sup>5</sup> Max-Planck-Institut für Extraterrestrische Physik, Garching, Germany

<sup>6</sup> Department of Physics, Yale University, P.O. Box 201820, New Haven, CT 06520-8120, USA

<sup>7</sup> Yale Center for Astronomy and Astrophysics, P.O. Box 208121, New Haven, CT 06520, USA

<sup>8</sup> Harvard-Smithsonian Center for Astrophysics, 60 Garden Street, Cambridge, MA 02183, USA

<sup>9</sup> Institute for Astronomy, University of Edinburgh, Royal Observatory, Blackford Hill, Edinburgh EH9 3HJ, UK

Received 2018 November 2; revised 2019 February 25; accepted 2019 March 13; published 2019 May 1

## Abstract

We report the results of a Sloan Digital Sky Survey IV eBOSS program to target X-ray sources and mid-infrared-selected *Wide-field Infrared Survey Explorer* (*WISE*) active galactic nucleus (AGN) candidates in a  $36.8 \text{ deg}^2$  region of Stripe 82. About half this survey ( $15.6 \text{ deg}^2$ ) covers the largest contiguous portion of the Stripe 82 X-ray survey. This program represents the largest spectroscopic survey of AGN candidates selected solely by their *WISE* colors. We combine this sample with X-ray and *WISE* AGNs in the field identified via other sources of spectroscopy, producing a catalog of 4847 sources that is 82% complete to  $r \sim 22$ . Based on X-ray luminosities or *WISE* colors, 4730 of these sources are AGNs, with a median sample redshift of  $z \sim 1$ . About 30% of the AGNs are optically obscured (i.e., lack broad lines in their optical spectra). BPT analysis, however, indicates that 50% of the *WISE* AGNs at  $z < 0.5$  have emission line ratios consistent with star-forming galaxies, so whether they are buried AGNs or star-forming galaxy contaminants is currently unclear. We find that 61% of X-ray AGNs are not selected as mid-infrared AGNs, with 22% of X-ray AGNs undetected by *WISE*. Most of these latter AGNs have high X-ray luminosities ( $L_x > 10^{44} \text{ erg s}^{-1}$ ), indicating that mid-infrared selection misses a sizable fraction of the highest luminosity AGNs, as well as lower luminosity sources where AGN-heated dust is not dominating the mid-infrared emission. Conversely,  $\sim 58\%$  of *WISE* AGNs are undetected by X-rays, though we do not find that they are preferentially redder than the X-ray-detected *WISE* AGNs.

**Key words:** catalogs – galaxies: active – surveys

**Supporting material:** FITS file

## 1. Introduction

Active galactic nuclei (AGNs) serve as signposts of accreting supermassive black holes (SMBHs) across the universe. Multiwavelength selection of AGNs is necessary for a complete picture of SMBH growth and evolution, mitigating selection biases that are inherent in any one band. Optical AGN selection favors Type 1 AGNs, or those where we have a direct view of the accretion disk and associated broad-line region. The typical blue colors of these Type 1 AGNs and the point-like morphology serve as a basis for ground-based targeting from optical spectroscopic surveys, such as the Sloan Digital Sky Survey (SDSS; York et al. 2000), garnering hundreds of thousands of confirmed AGNs (e.g., Pâris et al. 2017). However, optical surveys are biased against obscured AGNs, where the accretion disk and broad-line region are hidden behind large amounts of dust and gas on circumnuclear to galactic scales. Though these Type 2 AGNs can be identified in nearby (i.e.,  $z < 0.5$ ) galaxies on the basis of the ratios of their narrow emission lines using the so-called “BPT” diagram (Baldwin et al. 1981), they are more challenging to efficiently detect at larger distances, requiring infrared spectroscopic follow-up to observe the traditional BPT emission lines (Kewley et al. 2013a, 2013b) or alternate diagnostics (Lamareille 2010; Trouille et al. 2011; Juneau et al. 2011).

X-rays, produced in a hot corona around the accretion disk, provide a direct probe of SMBH fueling. This energetic emission pierces through optically obscuring dust, but becomes attenuated at high gas column densities, especially at Compton-thick levels ( $N_H > 1.25 \times 10^{24} \text{ cm}^{-2}$ ), where they will appear X-ray weak (Bassani et al. 1999; Heckman et al. 2005; LaMassa et al. 2009, 2011), even at the highest X-ray energies (Lansbury et al. 2014, 2015).

AGN-heated dust emits at mid-infrared (MIR) energies, imparting a characteristic power-law shape to the spectral energy distribution (SED), dominating over host galaxy star formation in powerful AGNs (Lacy et al. 2004; Stern et al. 2005; Donley et al. 2012). MIR color selection then becomes a powerful tool to recover obscured AGNs missed by optical and X-ray selection, though contamination from star-forming galaxies can be considerable at fainter fluxes (Barmby et al. 2006; Cardamone et al. 2008; Mendez et al. 2013). Additionally, AGNs at fainter luminosities are missed by MIR selection (Mateos et al. 2012; LaMassa et al. 2016a; Menzel et al. 2016).

A combination of AGN samples selected via independent methods is then crucial to understanding selection effects and providing a comprehensive view of cosmic black hole growth. While survey fields like GOODS (Alexander et al. 2003;

Comastri et al. 2011; Xue et al. 2011; Luo et al. 2017) and COSMOS (Hasinger et al. 2007; Scoville et al. 2007; Elvis et al. 2009; Civano et al. 2016) have a wealth of multi-wavelength data where such analysis can be done, these cover a relatively small volume of the universe with survey areas of  $\sim 0.13 \text{ deg}^2$  and  $\sim 2.2 \text{ deg}^2$ , respectively. To find a representative sampling of rare AGNs, wide-area surveys, which cover a large volume of the universe, are necessary, complementing the AGN population found in smaller area fields.

Stripe 82X is such a wide-area X-ray survey, covering  $\sim 31 \text{ deg}^2$  of the legacy SDSS Stripe 82 field (LaMassa et al. 2013a, 2013b, 2016b; Ananna et al. 2017). Imaged  $\sim 100$  times as part of a supernova legacy program (Frieman et al. 2008), the coadded depth in Stripe 82 is approximately two magnitudes deeper than any single SDSS scan (Annis et al. 2014; Jiang et al. 2014; Fliri & Trujillo 2016). Stripe 82 contains rich multiwavelength coverage, with ultraviolet data from *GALEX* (Morrissey et al. 2007), near-infrared (NIR) data from UKIDSS (Hewett et al. 2006; Casali et al. 2007; Lawrence et al. 2007) and the Vista Hemisphere Survey (VHS; McMahon et al. 2013), MIR data from *Spitzer* IRAC (Timlin et al. 2016; Papovich et al. 2016) and *Wide-field Infrared Survey Explorer* (*WISE*; Wright et al. 2010), far-infrared coverage from *Herschel* SPIRE (Viero et al. 2014), and radio coverage at 1.4 GHz from FIRST (Becker et al. 1995; Helfand et al. 2015). About half ( $\sim 15.6 \text{ deg}^2$ ) of the Stripe 82X survey is contiguous, spanning  $14^\circ < \text{R.A.} < 28^\circ$  and  $-0^\circ.6 < \text{decl.} < 0^\circ.6$ . This region was observed between 2014 and 2015 with *XMM-Newton* in response to a successful AO13 proposal (PI: Urry; LaMassa et al. 2016b) and reaches a 0.5–10 keV flux limit of  $\sim 10^{-14} \text{ erg s}^{-1} \text{ cm}^{-2}$  at half the survey area.

This contiguous, homogeneously covered portion of the Stripe 82X survey provides an ideal data set to assess whether AGNs identified via various multiwavelength selection methods represent unique populations, to determine the types of AGNs common across identification methods, and to construct a bolometric quasar luminosity function to analyze how AGNs evolve over cosmic time. Important first steps are to determine redshifts and classifications for the X-ray sources via spectroscopy and to create an independent sample of MIR-selected AGNs in the same survey area. These samples can then be combined with optically selected AGNs from SDSS within this survey area for a multiwavelength view of black hole growth.

A special eBOSS (Smee et al. 2013; Dawson et al. 2016) program of SDSS-IV (Gunn et al. 2006; Blanton et al. 2017) spectroscopically observed the *XMM-Newton* AO13 Stripe 82X field, targeting 849 SDSS counterparts to Stripe 82 X-ray sources from the catalog of LaMassa et al. (2016b) and 1518 independently selected *WISE* AGN candidates (based on their  $W1 - W2$ ,  $3.4\text{--}4.6 \mu\text{m}$ , color; Assef et al. 2013) within the same survey area. In this catalog release paper, we describe the observations and success rate of the spectroscopic identifications. We combine this source list with other spectroscopically identified X-ray and *WISE* AGNs in the field to create a nearly complete sample of X-ray- and MIR-selected AGNs to  $r \sim 22$ , and we comment on the demographics of these populations. Throughout, we assume a cosmology of  $H_0 = 67.8 \text{ km s}^{-1} \text{ Mpc}^{-1}$ ,  $\Omega_m = 0.37$ ,  $\Omega_\Lambda = 0.69$  (Planck Collaboration et al. 2016).

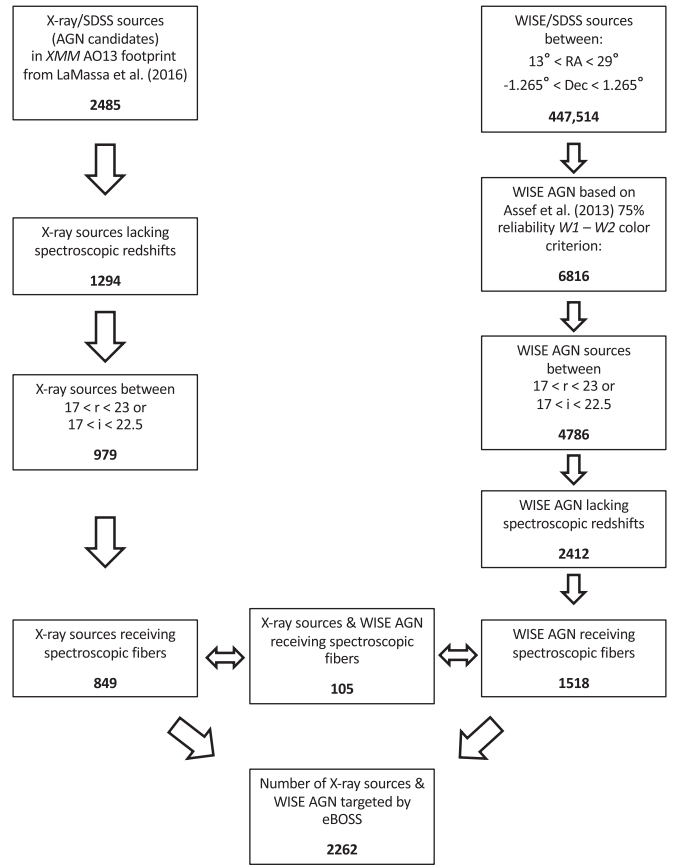


**Figure 1.** Flowchart that illustrates how the X-ray and *WISE* AGN spectroscopic candidates were chosen. Note that the published catalog was slightly modified from the target list to use SDSS counterparts to X-ray sources from the Ananna et al. (2017) Stripe 82X-multiwavelength catalog and to include *WISE* AGN candidates based on the updated color criteria of Assef et al. (2018).

## 2. Target Selection

The parent X-ray and *WISE* samples we used for the target selection are discussed in detail below. We identified SDSS counterparts to these sources using the maximum likelihood estimator (MLE; Sutherland & Saunders 1992), a statistical approach that accounts for the distance between an X-ray (*WISE*) source and potential multiwavelength counterparts within a predefined search radius, the magnitudes of the potential associations within that search radius, the magnitude distribution of background sources, and astrometric errors on the X-ray (*WISE*) coordinates and those of the potential multiwavelength counterparts. This algorithm computes a likelihood ratio (LR), which is the probability that the correct counterpart is found divided by the probability that an unassociated background source is there by chance. From LR, a reliability value ( $R$ ) is then calculated for each source. This counterpart matching was done separately for the X-ray and *WISE* sources, where  $R$  (LR) was used to distinguish between true counterparts and spurious associations for the X-ray (*WISE*) sources, as discussed below.

In total, 2262 SDSS counterparts to X-ray- and infrared-selected sources were targeted by the eBOSS Stripe 82X survey in the fall of 2015. Of these SDSS sources, 105 were both X-ray- and infrared- selected, 744 were detected only in X-rays, and 1413 were selected on the basis of their MIR properties alone. Figure 1 summarizes the selection criteria for

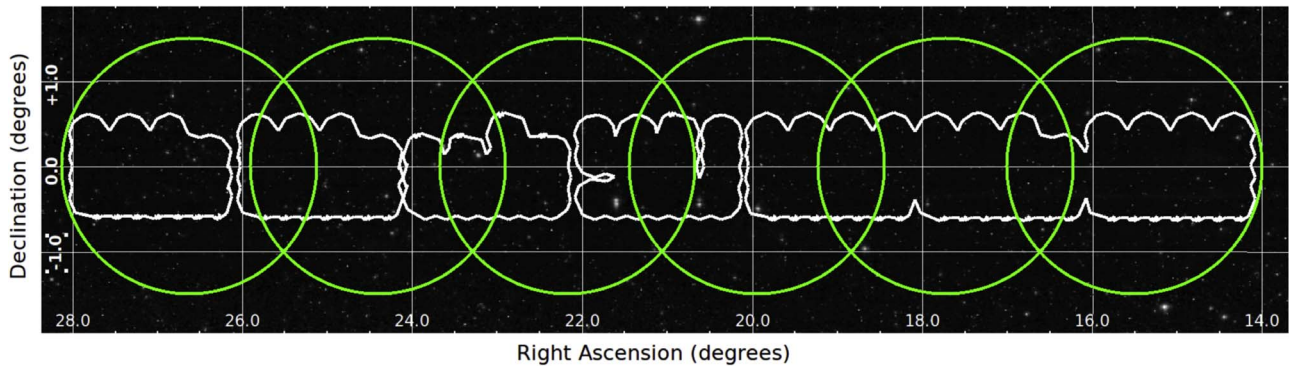


**Figure 2.** Layout of the field observed by the Stripe 82X eBOSS program. The green circles overlaid on the SDSS image mark the positions of the six SDSS-IV spectroscopic plates of this program. The size of each circle is  $3^\circ$  in diameter, corresponding to the field of view of the SDSS spectroscopic plates, which covers  $36.8 \text{ deg}^2$  of Stripe 82. The white polygon demarcates the region covered by the  $15.6 \text{ deg}^2$  AO13 *XMM-Newton* observations of the Stripe 82X survey (LaMassa et al. 2016b).

both classes of objects, with further details in the following subsections.

After the eBOSS observations, an updated multiwavelength catalog matched to the Stripe 82X survey was published in Ananna et al. (2017), using a deeper coadded SDSS catalog (Fliri & Trujillo 2016) and matches to *Spitzer* data in the field (Papovich et al. 2016; Timlin et al. 2016). Ananna et al. (2017) cross-matched these various multiwavelength associations and reported the most likely counterpart to each X-ray source, resulting in  $\sim 14\%$  discrepant associations compared with the LaMassa et al. (2016b) catalog. Additionally, Assef et al. (2018) published a *WISE* AGN catalog using slightly updated color selection criteria for the 90% and 75% reliability levels, leading to slight discrepancies between the eBOSS *WISE* AGN target list and the most up-to-date *W1* – *W2* AGN definition.

When discussing the targeting procedure and inspecting the results of the pipeline, we preserve the original source lists, since success of the pipeline depends on optical properties, regardless of why the source was included in the target list. However, we vet these lists to only retain the sources in the updated Ananna et al. (2017) catalog and those that obey the revised Assef et al. (2018) *W1* – *W2* color criterion at the 75% reliability level in the published catalog and when we comment on AGN demographics.

### 2.1. X-Ray

The X-ray sample is culled from the  $15.6 \text{ deg}^2$  portion of the  $31.3 \text{ deg}^2$  Stripe 82 X-ray survey that was observed with *XMM-Newton* in AO13 (LaMassa et al. 2016b). The full X-ray coverage in Stripe 82X includes  $\sim 4.6 \text{ deg}^2$  of *XMM-Newton* observations from AO10 and archival *XMM-Newton* and *Chandra* observations in the field (LaMassa et al. 2013a, 2013b) that were not observed with this SDSS-IV eBOSS spectroscopic program because the fields were mostly not contiguous with the *XMM-Newton* AO13 footprint. The X-ray-selected sources are from the *XMM-Newton* AO13 program, as well as two archival *Chandra* observations and one archival *XMM-Newton* observation that overlapped the footprint of the SDSS spectroscopic plates. The coverage of the eBOSS Stripe 82X survey region is somewhat larger than the  $15.6 \text{ deg}^2$  *XMM-Newton* AO13 survey area (see Figure 2).

The details of the MLE matching are discussed in LaMassa et al. (2013b, 2016b); in brief, SDSS associations were identified within a  $7''$  search radius of an *XMM-Newton* source (Brusa et al. 2010), or within  $5''$  of a *Chandra* source (Civano et al. 2012).

The X-ray sources were originally matched to both the SDSS single-epoch imaging catalog and the coadded SDSS catalogs of Jiang et al. (2014), which reach a depth of  $r \approx 24.6$  mag (AB), that is, about two magnitudes deeper than the SDSS single-epoch data: if a source was found in the SDSS single-epoch imaging, we retained that match to enable efficient querying of the web-based SDSS database, otherwise we reported the magnitude(s) from the coadded catalog (if a reliable counterpart was found in this deeper catalog). We empirically determined a reliability threshold above which we accepted an SDSS source as a counterpart to an X-ray source: we shifted the X-ray positions by random amounts, repeated the MLE counterpart matching, and defined a critical reliability cutoff where the spurious association fraction (i.e., matches to randomized positions) was  $\sim 10\%$  of the matches to actual X-ray sources. Any SDSS source with a reliability value above this threshold was considered an X-ray counterpart.

Within the SDSS-IV eBOSS Stripe 82X survey area, 2485 SDSS sources are identified as being counterparts to X-ray sources in LaMassa et al. (2016b). Of these, 1191 had preexisting spectroscopic redshifts, with 786 from previous SDSS programs (e.g., SDSS Data Releases DRs 8–13 and previous releases of the SDSS quasar catalog; Abazajian et al. 2009; Aihara et al. 2011; Alam et al. 2015; Albareti et al. 2017) and the remainder from 2SLAQ (Croom et al. 2009), 6dF (Jones et al. 2004, 2009), and proprietary SDSS redshifts at the time the target list was generated (which are now publicly available in SDSS DR 14; Abolfathi et al. 2018). Of the 1294 X-ray/SDSS sources lacking redshifts, we imposed the following magnitude cuts to maximize the success rate of the SDSS-IV eBOSS program,  $17 < r < 23$  or  $17 < i < 22.5$ , leaving us with 979 sources in the parent target list. Of these sources, 849 received fibers during the tiling process. Figure 3 shows the *r*-band magnitude distribution of the sample of the SDSS counterparts to X-ray sources within the SDSS-IV eBOSS Stripe 82X survey footprint, highlighting the sources with preexisting SDSS spectroscopy that were public at the time of the observations and those targeted by the eBOSS survey.

### 2.2. Mid-infrared

The starting point for the MIR selection of AGNs was the ALLWISE DR catalog (hereafter *WISE*), which combines data from the *WISE* cryogenic and NEOWISE missions (Mainzer et al. 2011), as well as the postcryogenic survey phases. Since



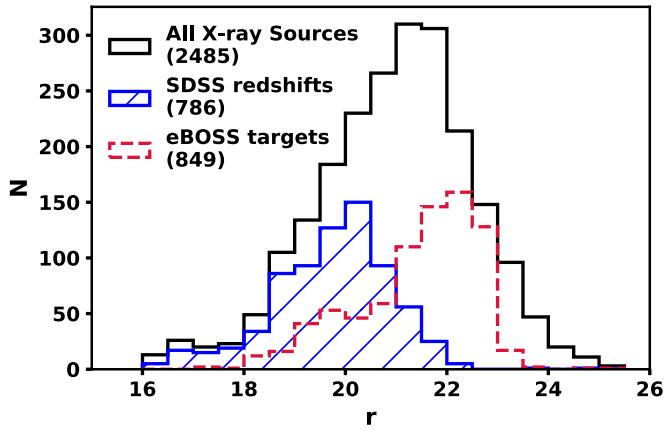


**Figure 3.** SDSS  $r$ -band optical magnitude distribution of the X-ray sources within the Stripe 82X *XMM-Newton* AO13 footprint (solid black histogram), with the subset of sources having preexisting public spectroscopic redshifts from SDSS (blue hatched histogram) and targeted by this eBOSS program (red dashed histogram) highlighted; an additional 405 SDSS/X-ray sources have redshifts from other surveys and SDSS data that were proprietary at the time of the observations. The eBOSS targets are generally fainter than those with existing spectroscopy.

the circular SDSS spectroscopic plates have a diameter of  $3^\circ$ , six plates were needed to cover the width of the *XMM-Newton* AO13 Stripe 82X strip (see Figure 2). The SDSS plates cover a greater area than the *XMM-Newton* AO13 footprint ( $36.8 \text{ deg}^2$ ), and the exact tiling strategy was only finalized after the parent target lists were generated. Hence, the *WISE* target list was chosen to cover the general area of the SDSS plates, with the exact targets chosen in the tiling process.

To create this master list, we selected *WISE* sources with right ascensions of  $13^\circ \leq \text{R.A.} \leq 29^\circ$  and declinations of  $-1.265 \leq \text{decl.} \leq 1.265$ , which correspond to the approximate width of Stripe 82 where deep coadded optical photometry is available. We further excluded potentially spurious *WISE* sources and sources with MIR photometry or positions affected by image artifacts by requiring that the contamination and confusion flag (CC\_FLAGS) of the *WISE* catalog equals zero in all four *WISE* spectral bands.

These selections yield a total of 543,584 *WISE* sources. These are matched to optical counterparts using the Stripe 82 coadded catalogs presented by Jiang et al. (2014), using the MLE methodology as implemented in Brusa et al. (2007). The maximum radius within which potential counterparts are searched for is set to  $2''$ . This limit is motivated by the subarcsecond positional accuracies of both the *WISE* and Jiang et al. (2014) catalogs. An LR cut of  $\text{LR} > 0.2$  is adopted for the *WISE* optical counterparts, which yields identifications for 82% of the *WISE* sample (447,514 sources) with an expected spurious fraction of  $< 3\%$ .

Figure 4 presents the  $r$ -magnitude distribution of the *WISE* optical counterparts; 39,559 SDSS counterparts were not detected in the  $r$  band and are thus not included in this plot. Also shown in this figure is the distribution for 6110 *WISE* AGN candidates with  $r$ -band detections and *WISE*  $W1 - W2$  colors redder than the 75% reliability color cut defined by Assef et al. (2013), as shown in Figure 5; an additional 706 *WISE* AGNs are not shown since they lack  $r$ -band detections. These sources have a bimodal  $r$ -band magnitude distribution. The optically faint peak of the distribution in Figure 4 may include a large fraction of obscured AGNs (e.g., DiPompeo et al. 2014), where the optical range of the spectral energy

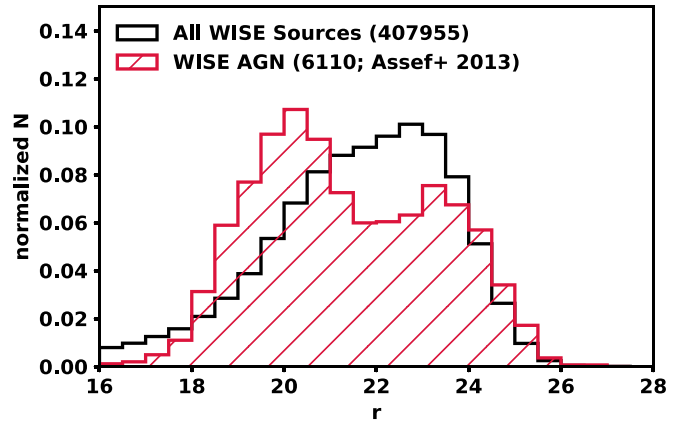


**Figure 4.**  $r$ -band optical magnitude distribution of the SDSS counterparts to the *WISE* sources in the Stripe 82 subregion that brackets the approximate area covered by this SDSS-IV eBOSS Stripe 82X program ( $13^\circ \leq \text{R.A.} \leq 29^\circ$ ,  $-1.265 \leq \text{decl.} \leq 1.265$ ). The optical photometry is from Jiang et al. (2014). The black histogram is for all *WISE* sources in the area, while the red hatched histogram shows the magnitude distribution of the *WISE* AGN subsample selected using the  $W1 - W2$  color selection for 75% reliability from Assef et al. (2013); there are additional *WISE* sources and *WISE* AGNs not shown here because they were not detected in the  $r$  band in the Jiang et al. (2014) catalog.

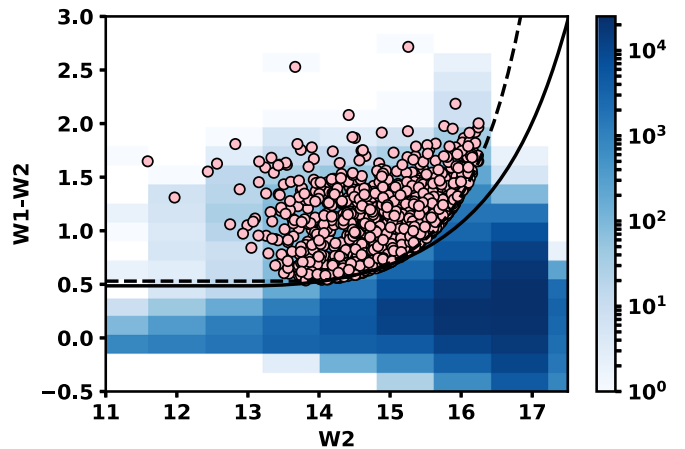


**Figure 5.** *WISE*  $W1 - W2$  color vs.  $W2$  magnitude for *WISE* sources within the SDSS-IV eBOSS Stripe 82X target area that obey the optical magnitude cuts in the main text ( $r < 23$  or  $i < 22.5$ ). The dashed line indicates the Assef et al. (2013)  $W1 - W2$  color cut for 75% reliability, which was used to make the target list; the solid line shows the revised Assef et al. (2018) criterion, which we use to generate the final catalog and to comment on source demographics. The targets are shown by the pink circles overlaid on the total number of *WISE* sources, as indicated by the color bar.

distribution is dominated by the host galaxy rather than AGN light.

Targets for follow-up spectroscopy were selected to lie within the 75% reliability *WISE*  $W1 - W2$  color wedge defined by Assef et al. (2013; see Figure 5) and have optical counterparts with magnitudes brighter than  $r = 23$ , or  $i = 22.5$  mag, in the Jiang et al. (2014) coadded catalog, leaving 4786 sources. These optical limits are a trade-off between depth, to explore the nature of the optically faint *WISE* AGN candidates (e.g., Figure 4), and sufficient signal-to-noise ratio (S/N) of the resulting SDSS spectra to measure reliable redshifts, at least in the case of emission line galaxies or AGNs (Menzel et al. 2016; Delubac et al. 2017; Raichoor et al. 2017). Spectroscopy is available for 2374 of the *WISE* AGNs from previous SDSS programs. These sources were not targeted as

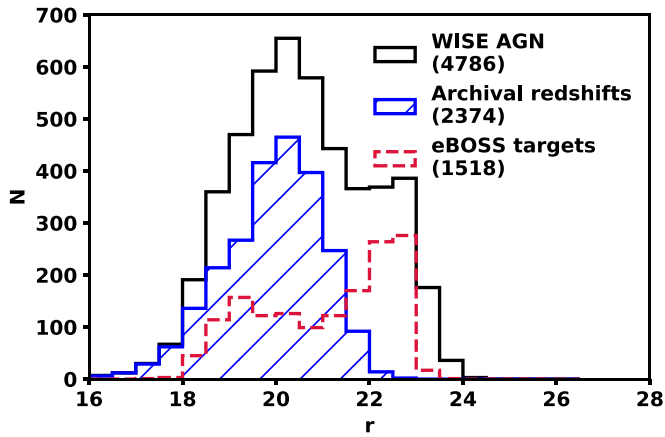


**Figure 6.**  $r$ -band optical magnitude distribution of the *WISE* AGNs that are selected using the 75% reliability criterion of Assef et al. (2013), spatially overlap the targeting region of the SDSS-IV eBOSS Stripe 82X program, and are brighter than  $r < 23$  or  $i < 22.5$  (black solid histogram). The blue hatched histogram corresponds to sources with spectroscopy from SDSS programs prior to this eBOSS survey, and the red dashed region shows the magnitude distribution of the *WISE* AGN candidates that received fibers in the SDSS tiling process and were thus targeted by the eBOSS program.

*WISE*-selected AGNs in the eBOSS survey unless they qualified for repeat observations to explore QSO optical spectral variability (see Section 2.3). The remaining 2412 sources were potential spectroscopic targets as *WISE* AGN candidates; 1518 received fibers in the tiling process. The optical magnitude distribution of these sources is shown in Figure 6.

### 2.3. Additional Targets

Additional sources were added to the target list to make use of all available spectroscopic fibers during the tiling process (see Table 1 for a summary). These “filler” targets included the following:

1. Quasar candidates from the photometric redshift catalogs of
  - (a) Richards et al. (2015), using SDSS and *WISE* photometry (“S82X\_RICHARDS15\_PHOTOQSO\_TARGET”);
  - (b) Peters et al. (2015), using optical photometry and variability in Stripe 82 (“S82X\_PETERS15\_COLORVAR\_TARGET”);
2.  $z > 4$  quasar candidates from LSST (AlSayyad et al. 2015, “S82X\_LSSTZ4\_TARGET”);
3. Changing-look AGN candidates, where the optical spectra may show disappearing or emerging broad Balmer lines between spectroscopic epochs (e.g., Denney et al. 2014; Shappee et al. 2014; LaMassa et al. 2015; Ruan et al. 2016; Runnoe et al. 2016; Gezari et al. 2017; Yang et al. 2018), using the photometric variability cuts employed in MacLeod et al. (2016), with or without an additional cut on the timing of the previous spectral epoch (“S82X\_CLAGN1\_TARGET” or “S82X\_CLAGN2\_TARGET,” respectively);
4. *WISE* AGN candidates from *WISE* forced photometry at the positions of known SDSS sources (Lang et al. 2016) that were otherwise not already in the *WISE* target list (“S82X\_UNWISE\_TARGET”);

5. Photometric variability selected quasar candidates from Palanque-Delabrouille et al. (2016, “S82X\_SACLAY\_VAR”);
6. Quasar candidates selected on the basis of their SDSS and *Spitzer* colors, using a boosted decision-tree algorithm (“S82X\_SACLAY\_BDT”);
7. High-redshift quasar candidates identified by defining drop-out regions in optical color and optical-*WISE* color parameter space (“S82X\_SACLAY\_HIZ”; see Richards et al. 2002).

The SDSS counterparts to the X-ray sources and the *WISE* AGN candidates are listed as “S82X\_XMM\_TARGET” and “S82X\_WISE\_TARGET,” respectively, in Table 1 and in the SDSS database. We focus on these targets exclusively when commenting on the results of the eBOSS program, and we note that the spectra for the ancillary targets were made public in SDSS DR 14 (Abolfathi et al. 2018), with specific samples to be discussed in future papers (e.g., C. MacLeod et al. 2019, in preparation).

### 2.4. Tiling

The objective of the tiling process is to achieve a distribution of sources across a plate that maximizes the number of observed targets with a minimum number of plates (Dawson et al. 2016). As the X-ray and *WISE* target density was fairly uniform across the region, we chose to tile six plates with fixed centers (see Figure 2). These plates are identified with plate identification numbers ranging from 8788 to 8793. Target selection algorithms resulted in an average number of 1304 targets per plate. Five percent of these targets were eliminated either due to a possible knock-out with an allocated high-priority fiber or due to their high brightness.

While tiling the fibers across the plates, we opted to treat each plate independently so that there are repeat spectra of high-priority targets in the overlap regions. However, many targets are relatively bright ( $r < 22$ ), in which case the S/N in a nominal observation ( $\sim 2$  hr) would be sufficient (“S82X\_BRIGHT\_TARGET”). Hence, we adopted a tiered-priority system for assigning fibers to the targets. The advantage of this system is that we could free up some fibers for additional targets by removing the bright objects from the overlap regions as each plate is successively tiled. For each plate, we carried out three rounds of tiling, and in each round we assigned fibers to targets depending on the priority of the targets. Targets corresponding to “S82X\_XMM\_TARGET,” “S82X\_WISE\_TARGET,” “S82X\_LSSTZ4\_TARGET,” “S82X\_CLAGN1\_TARGET,” and “S82X\_CLAGN2\_TARGET” were included in the highest priority list. The next priority list includes targets corresponding to “S82X\_SACLAY\_VAR\_TARGET,” “S82X\_SACLAY\_BDT\_TARGET,” “S82X\_RICHARDS15\_PHOTOQSO\_TARGET,” and “S82X\_PETERS15\_COLORVAR\_TARGET.” The final priority list contains targets corresponding to “S82X\_BRIGHT\_TARGET,” “S82X\_SACLAY\_HIZ\_TARGET,” and “S82X\_UNWISE\_TARGET.” Table 1 lists the number of available targets and the number of tiled targets for the different target classes among the six plates. For each round, if all of the higher priority targets were assigned fibers, the remaining fibers were allocated to the targets in the next priority. Three hundred fifty-three targets have repeat spectra owing to the overlap of the plates.

**Table 1**  
SDSS Tiling Summary: Number and Fraction of Targets Receiving Spectroscopic Fibers on Each SDSS Plate<sup>a</sup>

TARGET CLASS	8788 $N_{\text{tot}} - N_{\text{tile}}$	8789 $N_{\text{tot}} - N_{\text{tile}}$	8790 $N_{\text{tot}} - N_{\text{tile}}$	8791 $N_{\text{tot}} - N_{\text{tile}}$	8792 $N_{\text{tot}} - N_{\text{tile}}$	8793 $N_{\text{tot}} - N_{\text{tile}}$
S82X_BRIGHT_TARGET	921–547	832–520	678–470	593–451	703–461	705–478
S82X_XMM_TARGET	198–187	197–178	142–132	75–71	169–162	208–195
S82X_WISE_TARGET	324–303	289–269	259–248	247–235	297–282	287–273
S82X_SACLAY_VAR_TARGET	273–157	249–155	249–193	278–254	241–181	263–1829
S82X_SACLAY_BDT_TARGET	274–155	241–166	228–175	205–183	197–146	207–133
S82X_SACLAY_HIZ_TARGET	154–18	132–16	103–24	83–19	120–17	118–25
S82X_RICHARDS15_PHOTQSO_TARGET	32–24	40–30	30–23	29–29	42–40	42–35
S82X_PETERS15_COLORVAR_TARGET	225–132	265–173	219–179	212–192	215–66	239–161
S82X_LSSTZ4_TARGET	27–27	18–18	23–23	27–27	19–19	25–25
S82X_UNWISE_TARGET	206–59	170–49	125–37	127–48	173–54	152–62
S82X_CLAGN1_TARGET	2–2	2–1	5–5	4–4	5–5	5–5
S82X_CLAGN2_TARGET	23–21	26–23	31–29	37–35	35–31	31–28
TOTAL	1497–900	1422–900	1228–900	1117–900	1282–900	1313–900

**Note.**

<sup>a</sup>  $N_{\text{tot}}$  is the total number of targets overlapping the plate and  $N_{\text{tile}}$  is the number of targets that received spectroscopic fibers.

More specifically, and relevant to this catalog release, a total of 849 X-ray sources and 1518 *WISE* AGN candidates received spectroscopic fibers in the tiling process: 744 sources were X-ray only, 1413 sources were *WISE* only, and 105 sources were both X-ray and *WISE* targets, for a total of 2262 unique SDSS sources receiving fibers. Optically faint X-ray and *WISE* AGN candidates in overlapping regions between the neighboring plates were observed for twice the nominal exposure time, for 95 X-ray sources and 92 *WISE* sources.

### 3. Observations

The six plates were observed to twice the depth of typical eBOSS observations from previous SDSS DRs (Dawson et al. 2016). A plate is exposed for 15 minutes per exposure, with the number of exposures repeated until the square of the signal-to-noise ratio,  $(S/N)^2$ , per pixel in all four cameras (two red and blue cameras for spectrograph one and spectrograph two) passed a predetermined  $(S/N)^2$  threshold. Standard eBOSS plates had an  $(S/N)^2$  threshold of 10 and 22 in the blue and red cameras, for an object with  $g = 22$  and  $i = 21$ , respectively (Dawson et al. 2016); here the magnitudes are measured through the SDSS spectroscopic fibers.

As the Stripe 82X targets are relatively fainter than previous eBOSS targets, the Stripe 82X plates were exposed to a higher  $(S/N)^2$  threshold of 20 and 44 for the red and blue cameras, respectively. While it required 19 exposures at 15 minutes per exposure for two plates (8790 and 8791), due to bad observing conditions, the remaining four plates had 8–12 exposures of 15 minutes apiece. All of the observed data were run through the full SDSS pipeline, IDLSPEC2D v5\_10\_0. IDLSPEC2D extracts the spectrum corresponding to each exposure and combines the individual spectra to give a combined high- $S/N$  spectrum for each target. While combining the individual spectra, the SDSS pipeline excludes those exposures that have  $(S/N)^2$  less than 20% of the  $(S/N)^2$  of the best exposure. The pipeline rejected five exposures for plate 8791, but none for any of the remaining five plates.

#### 3.1. Pipeline Processing

Both the *WISE*- and X-ray-selected targets of this eBOSS survey include a large fraction of optically faint sources (e.g.,

Figure 6), close to the spectroscopic limit of 2 m class telescopes. Visual inspection was therefore deemed necessary to control the quality of the redshift measurements and optical spectral classifications for individual sources. Visual inspection was performed with the SPECCY webtool as described in Dwelly et al. (2017).

The visual inspection of the *WISE* spectra proceeded in two stages. First, five human classifiers inspected the spectra observed on a single plate of the survey (plate number 8792, observed on Modified Julian Date, MJD, 57364). The classification included the determination of the source redshift, an assessment of the redshift measurement reliability/quality, and the assignment of a rough spectral class. The starting points of the visual inspection were the products of the SDSS spectral reduction pipeline version 5.10.0 (Bolton et al. 2012). These include among others a best-fit spectral template and the corresponding redshift for each source, as well as a warning flag (ZWARNING) raised in the case of bad, uncertain, or more generically problematic redshift fits. The classifiers were presented with the best-fit pipeline products and had to decide whether they agreed or not, modify the redshift if they deemed necessary, and assign a redshift quality flag (Z\_CONF) and a spectral class (CLASS\_PERSON). The possible values of the latter flags and their meaning are presented Table 2. The visual inspection process enforced agreement of all classifiers on the redshift, quality, and class of a given source. Discrepancies were discussed and settled in a reconciliation round, which resulted in a final list of redshifts for the sources targeted on plate number 8792 (MJD 57364).

Based on these results, two of the classifiers (A.G., S.L.) visually inspected the remaining *WISE*-selected AGN candidates (A.G.) and X-ray sources (S.L.) targeted by this eBOSS program; a third classifier (V.M.) reviewed uncertain redshifts for the X-ray sources, and all three resolved any discrepant classifications via additional visual inspection and discussion. In the analysis that follows, we use all redshifts with  $Z\_CONF \geq 2$ , that is, spectra with at least a single identified feature.

### 4. Results

Of the 2262 SDSS sources targeted, we verified or independently determined redshifts and classifications for 1769 objects (78% success rate), with 1602 sources where

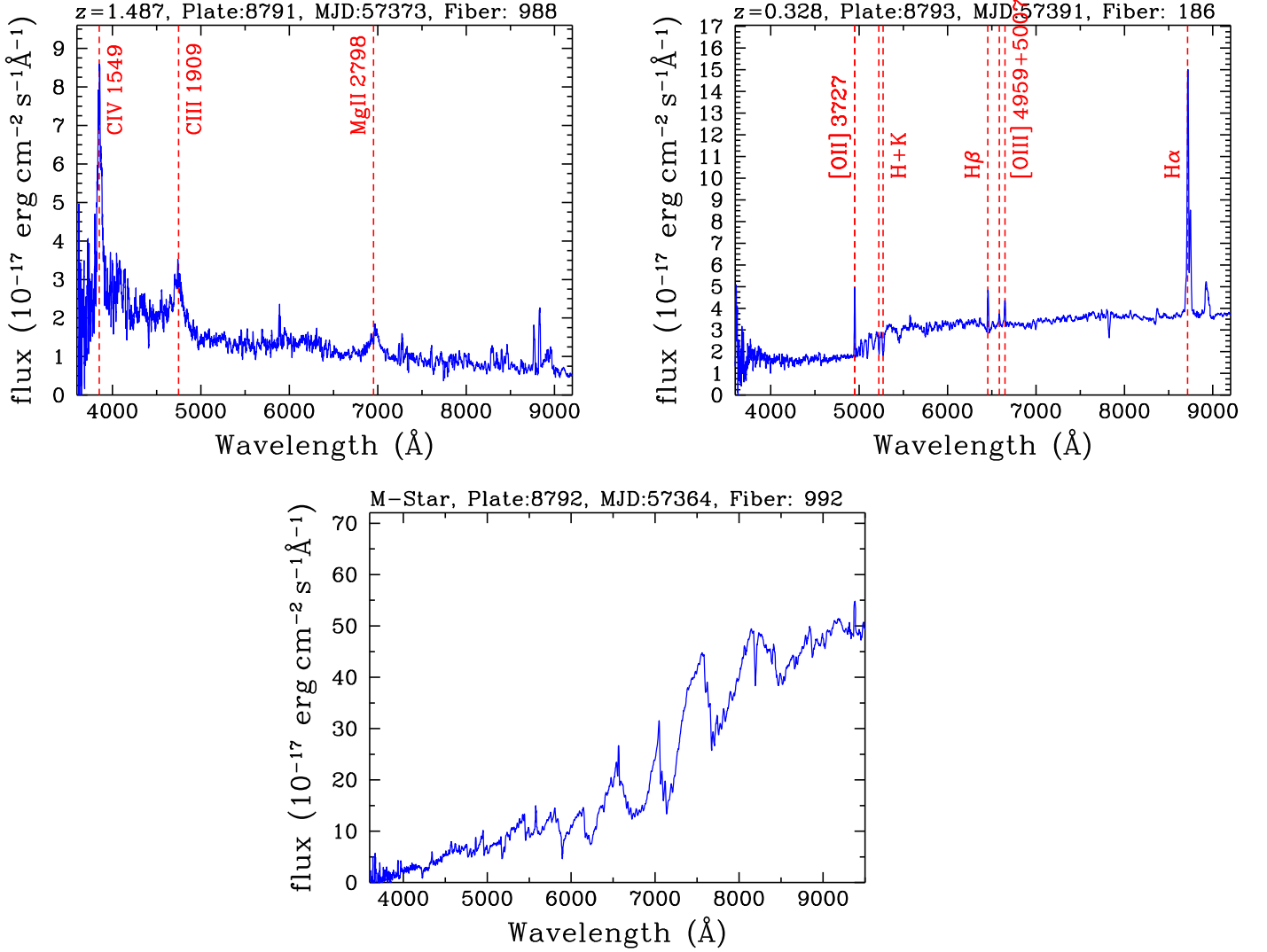


**Figure 7.** Example SDSS spectra of the various classes of objects detected in this eBOSS survey: (top left) Type 1 AGN at  $z = 1.487$  (MJD = 57373, fiber = 988, plate = 8791), (top right) SDSS galaxy at  $z = 0.328$  (MJD = 57391, fiber = 186, plate = 8793), and (bottom) star (M-Dwarf; MJD = 57364, fiber = 992, plate = 8792); notable transitions in the spectra of the extragalactic sources are indicated. All three objects were detected by both *WISE* and in X-rays. Both the QSO and galaxy have X-ray luminosities consistent with AGN and *WISE* W1 – W2 AGN colors at the 75% reliability threshold (Assef et al. 2013).

**Table 2**  
Visual Inspection Classification Scheme

CLASS_PERSON	Z_CONF			
	0	1	2	3
NONE	no vote/opinion	bad spectrum	no signal (continuum or spectral features)	continuum but no spectral features
QSO	...	...	single broad line	>1 spectral features (including broad lines)
Galaxy	...	...	single nonbroad line	>1 lines (nonbroad)
QSO BAL	...	...	BAL troughs only; uncertain $z$	BAL troughs and (narrow) emission lines
Blazar	...	...	continuum, no features to measure $z$	continuum and spectral features to measure $z$
Star	...	...	stellar-like continuum	stellar-like continuum and spectral features

$Z\_CONF = 3$  and 167 sources where  $Z\_CONF = 2$ . Of these sources, 591 are QSOs, 1129 are galaxies, and 49 are stars. We expect that the results from this eBOSS pilot program will inform observing strategies and efficient data quality-control checks for future SDSS surveys and those from other ground-based observatories.

We show an example spectrum of each of these sources in Figure 7 to highlight the variety of objects detected by the

eBOSS program; for reference, we include identifying information for these sources (MJD of observation, plate number, and fiber identification number) in the caption.

#### 4.1. Identification Success Rate

We explore the success rate of the pipeline as a function of optical magnitude in Figure 8, where we show the  $r$ -band



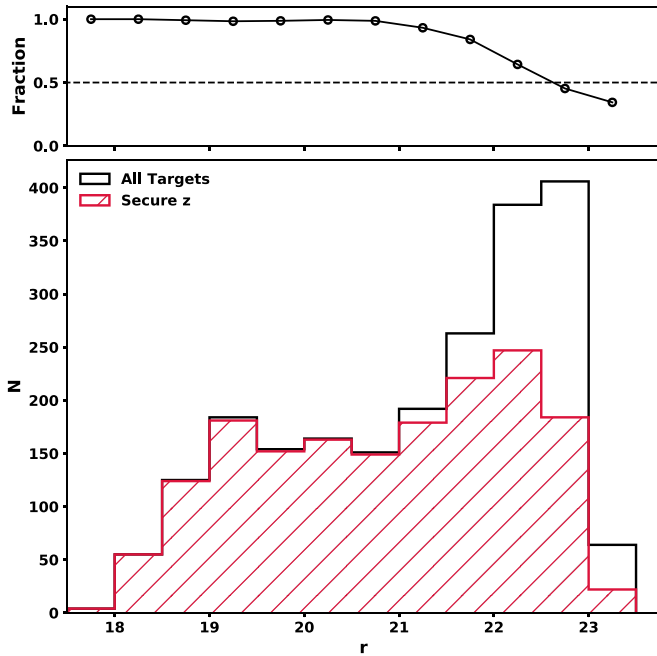


**Figure 8.** SDSS  $r$ -band optical magnitude (Jiang et al. 2014) distribution of the X-ray sources and *WISE* AGN candidates targeted by the eBOSS program. The solid black line shows all targets, while the red hatched histogram shows those sources that have reliable spectroscopic redshifts. The ratio of the two (i.e., the fraction of spectroscopic identifications as a function of  $r$  magnitude) is shown in the top panel; a horizontal line at 50% spectroscopic completeness is shown for reference. The fraction of identified sources drops below 50% at  $r > 22.5$ .

magnitude distribution for all targets (solid black histogram) and the subset with reliable redshifts (red hatched histogram; here we use the coadded optical photometry from Jiang et al. 2014 for all sources). The top panel of Figure 8 shows the fraction of sources identified as a function of their  $r$  magnitude, with a horizontal line at 50% completeness shown for reference.

We can identify more than half of the sample at  $r < 22.5$ . Even at the faintest magnitude limits (i.e.,  $22.5 < r < 23.5$ ), we are able to obtain reliable redshifts and classifications for above 37% of the sample, which is a significant fraction.

This success rate suggests that future SDSS programs can relax the nominal limiting magnitude constraint (e.g.,  $r < 22$  in the eBOSS quasar survey; Myers et al. 2015) for deeper observations and targets expected to have emission lines, akin to the Stripe 82X eBOSS survey. Our results indicate that surveys from observatories that have larger aperture mirrors, like the 4 m Dark Energy Survey, will also be successful in obtaining spectroscopic redshifts for sources to faintness levels of  $r \sim 24$  under similar observing conditions.

#### 4.2. Pipeline versus Visual Inspection: Clues from Pipeline Flags

In addition to the 493 sources where we were unable to determine a reliable redshift, we find spectroscopic redshifts that are different from the pipeline value for 73 sources (see Figure 9). Furthermore, for 54 sources where the pipeline redshift agrees with that from visual inspection, we found different spectroscopic classifications: either the pipeline failed to identify a weak, broad emission line apparent by eye and labeled a source a “Galaxy” instead of a “QSO,” or vice versa.

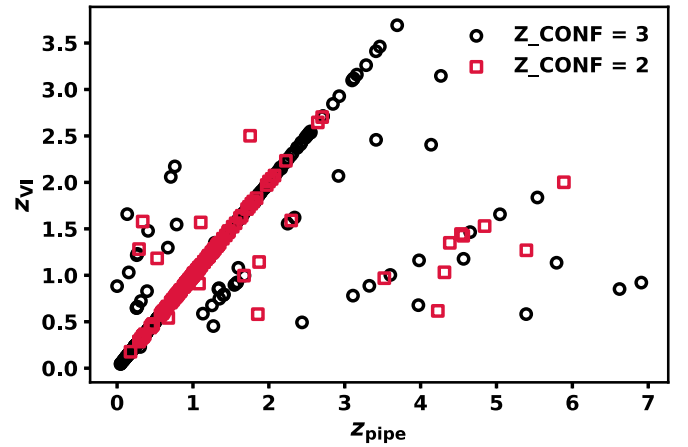


**Figure 9.** Comparison of pipeline redshifts ( $z_{\text{pipe}}$ ) and those verified or recalculated via visual inspection of the SDSS spectra ( $z_{\text{vl}}$ ) for extragalactic sources whose redshifts could be determined. We find redshifts discrepant from those produced by the pipeline in 73 sources (69 extragalactic sources and four stars misclassified as QSOs or galaxies by the SDSS pipeline); an additional 54 sources had consistent redshifts between the pipeline and visual inspection, but different classifications. We highlight the sources with red boxes where the redshift identification is less confident (i.e.,  $Z_{\text{CONF}} = 2$ ); the outliers are not predominantly the lower-confidence redshifts.

In total, we find 1642 sources (73% of targets) whose pipeline produced spectroscopic redshifts and classifications were deemed to be reliable via visual inspection. When considering the subset of 167 sources with lower confidence on the visually inspected redshift (i.e.,  $Z_{\text{CONF}} = 2$ ), we find that only 18 objects have redshifts discrepant from the pipeline value.

A nonnull value of the SDSS ZWARNING flag indicates potential problems with the pipeline fit to the SDSS spectrum. In 595 cases, the ZWARNING flag was set: 414 of the 493 sources where we were unable to determine a redshift had a nonnull ZWARNING value. About 30% of the sources flagged by the ZWARNING field did have spectra of sufficient quality to determine a redshift and classification. In 61 out of the 127 cases where we found a different redshift or spectroscopic classification than the pipeline, the ZWARNING flag was also nonnull.

Is there a way to immediately identify the remaining 145 sources where the pipeline redshift or classification was found to be unreliable via visual inspection, but the ZWARNING flag did not indicate a potential error? We look at the S/N of the spectrum for clues. In Figure 10, we plot the S/N for sources where the ZWARNING flag was null for the following subsets: visual inspection confirmed the pipeline-determined redshift and classification, we were able to determine a redshift from visual inspection that differed from that calculated by the pipeline, and we were unable to measure a redshift from the spectrum. As expected, the sources where we were unable to determine a redshift have the lowest S/N spectrum, while the sources where visual inspection revealed a different redshift from the pipeline have a range of S/N values.

Our results indicate that in the absence of the automated ZWARNING flag raising an alarm that the spectral fit may be problematic, the S/N can be used as a proxy. Seventy-eight of the 79 sources with spectra that were unidentifiable but had the ZWARNING flag set to null have S/N values below 2.25. About 60% of the sources (39 out of 66) where visual inspection revealed a redshift different from the pipeline are also below



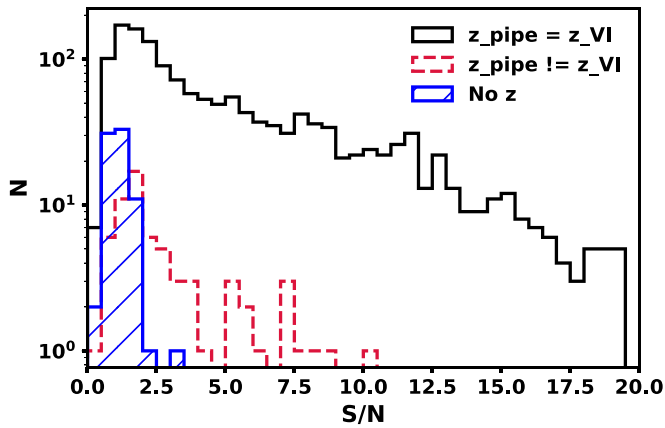


**Figure 10.** Signal-to-noise ratio distribution of sources where the ZWARNING flag was null. Most of the unidentifiable sources (blue hatched histogram) have S/N values below 2.25, as do  $\sim 60\%$  of the sources where the pipeline redshift ( $z_{\text{pipe}}$ ) disagrees with that from visual inspection ( $z_{\text{VI}}$ ; red dashed histogram), suggesting that sources whose spectra have S/N below this threshold warrant visual inspection. The black solid line represents the distribution for sources where visual inspection deemed that the pipeline redshift and classification were reliable.

this S/N limit. This S/N cut could potentially be used to automatically reject any spectral classifications below this threshold. However, 509 sources whose pipeline redshifts were deemed reliable via visual inspection (i.e., 29% of identified sources) would be discarded with such an automatic cut.

To balance the competing demands of maximizing sample size with reliable spectral classifications and limited resources, we suggest that visual inspection of any source where ZWARNING is nonnull or  $S/N < 2.25$  would be prudent. Though most of the spectra will be unclassifiable when the ZWARNING flag is set, about 30% of the sources should be recoverable with visual inspection. About 20% of sources that are not flagged as potentially problematic by the ZWARNING output and have  $S/N < 2.25$  are either unclassifiable or have different redshifts or classifications than the pipeline. Conversely, sources whose spectra are not flagged by ZWARNING and have  $S/N > 2.25$  have largely reliable pipeline measurements: only 27 out of 1040 sources ( $\sim 3\%$ ) that meet these criteria have different redshifts or classification from the pipeline.

#### 4.3. Creating the Spectroscopic Sample

As mentioned earlier, revised SDSS counterparts to the Stripe 82 X-ray sources (Ananna et al. 2017) and W1 – W2 AGN color selection criteria (Assef et al. 2018) were published after the eBOSS Stripe 82X observations. To ensure we are using the most up-to-date information, with the most reliable counterparts and current MIR AGN definition, we only retain X-ray and WISE AGN targets that are marked as X-ray counterparts in the catalog of Ananna et al. (2017) or WISE AGN candidates that obey the Assef et al. (2018) W1 – W2 color selection at the 75% level. Our catalog is further vetted to only include eBOSS sources for which we were able to verify or independently determine a redshift ( $Z_{\text{CONF}} \geq 2$ ).

To create a complete spectroscopic catalog of X-ray sources and WISE AGNs within this portion of the Stripe 82X survey, we include spectroscopic redshifts of SDSS counterparts to X-ray sources and WISE AGNs from the following sources:

1. Ancillary eBOSS Stripe 82X targets that are X-ray and WISE AGN counterparts based on these updated definitions (23 sources, for 1723 sources total from the SDSS-IV eBOSS Stripe 82X program);
2. Sources whose spectra became available in SDSS DR 14 but were not targeted as part of the SDSS-IV eBOSS Stripe 82X survey (1670 sources; Abolfathi et al. 2018; Pâris et al. 2018);
3. Previous SDSS DRs whose *zwarning* flag is null (Abazajian et al. 2009; Aihara et al. 2011; Ross et al. 2012; Alam et al. 2015; Albareti et al. 2017; Pâris et al. 2017) or whose spectra were independently vetted in a previous release of the Stripe 82X catalog (1407 sources; LaMassa et al. 2017);
4. 2SLAQ (29 sources; Croom et al. 2009);
5. 6dF (two sources; Jones et al. 2004, 2009);
6. Dedicated follow-up observing programs led by the members of the Stripe 82X collaboration (16 sources).

In total, our spectroscopic sample consists of 4847 sources, out of a parent sample of 10,702 X-ray and WISE AGN candidates that lie within the SDSS-IV eBOSS Stripe 82X survey footprint. In the spectroscopic sample, we have 1891 X-ray sources, 3657 WISE sources, and 701 sources that are both.

Before discussing the completeness of the relative samples, we note that a subset of sources that lie along the north–south border of the SDSS scans within Stripe 82 lack photometry in the Jiang et al. (2014) catalog (see their Figure 1). While creation of the eBOSS target list for the WISE AGN candidates was based on photometry from the Jiang et al. (2014) catalog, we supplement this information with SDSS single-epoch photometry for both the spectroscopic sample and the parent sample. The sources with photometry from the SDSS single-epoch imaging are a small percentage of the total, amounting to 3.8% of the spectroscopic sample and 5.2% of the parent sample, respectively.

With the caveat in mind that we are using photometry from two different catalogs, we estimate the spectroscopic completeness of our samples based on the *r*-band magnitude. We highlight that 12.5% of sources in the parent sample do not have photometric measurements in the *r* band. Based on inspecting the magnitude distributions of these sources at other optical wavebands, we see that the *r*-band dropouts are likely undetected as they are fainter than the *r*-band limit of the survey. We only consider the spectroscopic completeness for the subset of sources that are detected in the *r* band, noting that this value is an upper limit for the full sample, but reasonable to the *r*-band depth of the Jiang et al. (2014) catalog ( $r \sim 24.6$ ).

In Figure 11, we show the number of X-ray sources and WISE AGNs with spectroscopic redshifts compared with their parent samples as a function of *r*-band magnitude. We immediately see that the relatively low spectroscopic completeness of 45% for the combined sample is due to the bimodal distribution in the *r*-band magnitudes for the WISE sources, where there is an optically faint population that peaks at  $r \sim 24$ . When considering the samples separately, we find that the X-ray sample is 74% complete, while the WISE sample is 41% complete. Considering the *r*-band limit of the eBOSS Stripe 82X survey ( $r \sim 23$ ), the spectroscopic completeness rises to 72% for the full sample, and 82% and 71% for the X-ray and WISE samples, respectively. At  $r \sim 22$ , the combined sample is 82% complete, with the X-ray sample

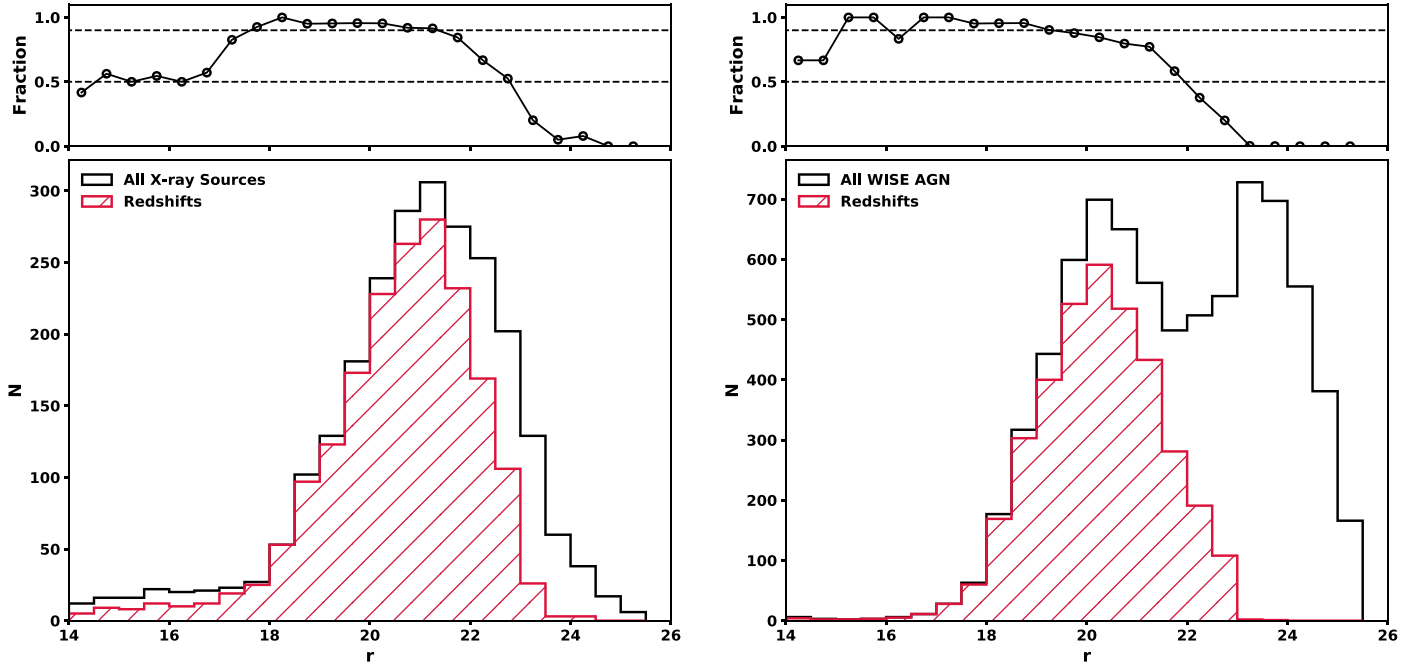


**Figure 11.**  $r$ -band distribution of the parent sample of X-ray (left) and *WISE* sources (right) within the SDSS-IV eBOSS Stripe 82X survey area (black histogram), with those having spectroscopic redshifts shown by the red hatched histogram. The fraction of sources with spectroscopic identifications in the corresponding  $r$ -band magnitude bins is shown in the top plot, with horizontal lines indicating 90% and 50% completeness. Up to  $r \sim 23$  (the magnitude limit of the eBOSS Stripe 82X survey), the X-ray sample is 82% complete and the *WISE* AGN sample is 71% complete. This completeness increases to 88% and 82% at  $r \sim 22$  for the X-ray and *WISE* AGN sample, respectively.

being 88% complete and the *WISE* sample being 82% complete.

#### 4.4. Description of Multiwavelength Information in the Catalog

In the catalog, we list the redshifts and optical spectroscopic classifications from the various surveys. The source of the spectroscopic redshift is noted in the column “*z\_src*” (see Table 3). If the redshift is from the SDSS-IV eBOSS Stripe 82X survey, the confidence on the vetted redshift is reported in “*z\_conf*,” as described in Table 2, otherwise it is set to a null value. The “*opt\_src*” column indicates whether the optical photometry is from the Jiang et al. (2014) catalog or the SDSS pipeline. If the former, the magnitudes represent the “AUTO” magnitude from SExtractor (i.e., Kron-like elliptical aperture). If the source is not detected in the Jiang et al. (2014) catalog but has photometric measurements in the single-epoch SDSS catalog, then the optical magnitudes are the ModelMags from the SDSS pipeline, which for extended sources represent the better of an exponential profile fit or a de Vaucouleurs profile fit, while a point-spread function (PSF) model is used for point sources. The *WISE* magnitudes measured from profile-fitting photometry are also reported if the source is detected by *WISE*. We include the *WISE* photometry for every X-ray source detected by *WISE*, regardless of whether the source has  $W1 - W2$  AGN colors.

For the X-ray sources, we report the flux in the soft (0.5–2 keV), hard (2–10 keV for *XMM-Newton*; 2–8 keV for *Chandra*), and full (0.5–10 keV for *XMM-Newton*; 0.5–8 keV for *Chandra*) bands, as well as the significance of the detection in the corresponding “*soft\_detml*,” “*hard\_detml*,” and “*full\_detml*” columns (LaMassa et al. 2016b), where  $\det\_ml = -\ln P_{\text{random}}$ , with  $P_{\text{random}}$  as the Poissonian probability that the detection is a

random fluctuation. For the energy bands where  $\det\_ml \geq 10$  (i.e.,  $P_{\text{random}} = 4.5 \times 10^{-5}$ ,  $4\sigma$  detection significance), we calculated the  $k$ -corrected X-ray luminosity<sup>10</sup> for extragalactic sources. We emphasize that the reported X-ray sensitivity of the Stripe 82X survey is calculated for a higher significance value, namely for  $\det\_ml \geq 15$  ( $5.1\sigma$ ) for the *XMM-Newton* observations and  $4.5\sigma$  for the archival *Chandra* observations.

From the X-ray fluxes, we calculated a hard-band X-ray luminosity ( $L_X$ ), which we use to classify whether a source is an X-ray AGN ( $L_X > 10^{42} \text{ erg s}^{-1}$ ; Brandt & Hasinger 2005; Brandt & Alexander 2015). If the hard-band X-ray flux is measured at  $\det\_ml \geq 10$ , then we use this luminosity as  $L_X$ . Otherwise, if the full-band detection is significant at the  $\det\_ml \geq 10$  level, we scale the full-band  $k$ -corrected luminosity by 0.665 to convert from the 0.5–10 keV band to the 2–10 keV band and estimate  $L_X$ . If both the hard- and full-band detections are not significant at this level, then the soft-band flux is scaled by a factor of 1.27 to convert from the 0.5–2 keV band to the 2–10 keV band for an estimate of  $L_X$ .

In the catalog, we include the  $W1 - W2$  colors for sources detected by *WISE*. We also note whether the source would be classified as an AGN at the 90% (“*WISE\_AGN\_90*”) or 75% (“*WISE\_AGN\_75*”) reliability level based on the criteria in Assef et al. (2018):

$$W1 - W2 > \begin{cases} \alpha_R \exp\{\beta_R(W2 - \gamma_R)^2\}, & W2 > \gamma_R \\ \alpha_R, & W2 \leq \gamma_R, \end{cases} \quad (1)$$

where  $(\alpha_R, \beta_R, \gamma_R) = (0.650, 0.153, 13.86)$  for the 90% reliability selection and  $(\alpha_R, \beta_R, \gamma_R) = (0.486, 0.092, 13.07)$

<sup>10</sup>  $L_{k\text{-corr}} = L_{\text{observed}} \times (1 + z)^{\Gamma-2}$ , where  $\Gamma$  is the power-law slope of the X-ray spectrum. For the Stripe 82X survey, we assumed  $\Gamma = 1.7$  for the hard and full bands and  $\Gamma = 2.0$  for the soft band (see LaMassa et al. 2013a, 2016b).

**Table 3**  
Stripe 82X eBOSS Value-added Catalog Column Descriptions

Column Name	Description
SDSS R.A.	SDSS R.A. (J2000)
SDSS Decl.	SDSS Decl. (J2000)
Plate	Plate number of SDSS spectroscopic observation; only applicable to sources with SDSS spectroscopy
MJD	Modified Julian date of SDSS spectroscopic observation; only applicable to sources with SDSS spectroscopy
Fiber	Fiber ID number of SDSS spectroscopic target; only applicable to sources with SDSS spectroscopy
Redshift	Spectroscopic redshift. If spectrum was derived from the SDSS-IV eBOSS Stripe 82X program, it was vetted or independently determined by visual inspection.
Class	Optical spectroscopic classification, vetted via visual inspection. Entries are “STAR,” “QSO” (if at least one broad emission line is present), “GALAXY” (only narrow emission lines or absorption lines are present).
z_src	Source of spectroscopic redshift and classification: 1. eBOSS_S82X: eBOSS spectroscopic survey of Stripe 82X, described in this paper; 2. SDSS_DR14: SDSS Data Release 14 (Abolfathi et al. 2018); 3. SDSS_DR14Q: SDSS Quasar Catalog Data Release 14 (Pâris et al. 2018); 4. SDSS_DR13: SDSS Data Release 13 (Albareti et al. 2017); 5. SDSS_DR12: SDSS Data Release 12 (Alam et al. 2015); 6. SDSS_DR12Q: SDSS Quasar Catalog Data Release 12 (Pâris et al. 2017); 7. SDSS_DR8: SDSS Data Release 8 (Aihara et al. 2011); 8. SDSS_DR7Q: SDSS Quasar Catalog Data Release 7 (Abazajian et al. 2009); 9. SDSS_zwarning_verified_by_eye: SDSS <i>zwarning</i> flag was nonnull, but spectrum was vetted in the catalog release of LaMassa et al. (2016b); 10. pre-BOSS: pre-BOSS pilot survey using Hectospec on MMT (Ross et al. 2012); 11. 2SLAQ: 2SLAQ survey (Croom et al. 2009); 12. 6dF: 6dF survey (Jones et al. 2004, 2009); 13. HYDRA_2014_Jan: follow-up observations of Stripe 82X sources from WIYN HYDRA in 2014 January, first published in LaMassa et al. (2016b); 14. HYDRA_2015_Jan: follow-up observations of Stripe 82X sources from WIYN HYDRA in 2015 January, first published in LaMassa et al. (2016b); 15. Gemini_GNIRS_2015: follow-up observations of obscured AGN candidates in Stripe 82X from Gemini GNIRS in 2015, first published in LaMassa et al. (2017); 16. DBSP_2015_Sep: follow-up observations of Stripe 82X sources from Palomar DoubleSpec in 2015 September, published here for the first time; 17. DBSP_2016_Aug: follow-up observations of Stripe 82X sources from Palomar DoubleSpec in 2016 August, published here for the first time; 18. DBSP_2017_Oct: follow-up observations of Stripe 82X sources from Palomar DoubleSpec in 2017 October, published here for the first time; 19. Keck_LRIS_Oct2017: follow-up observations of Stripe 82X sources from Keck LRIS in 2017 October, published here for the first time.
z_conf	Confidence on spectroscopic redshift via visual inspection. 2: one emission/absorption line identified, 3: $\geq 2$ emission/absorption lines identified; only applicable to sources from the SDSS-IV eBOSS Stripe 82X program
u_mag	SExtractor “AUTO” (i.e., Kron-line elliptical aperture) <i>u</i> -band magnitude from coadded Jiang et al. (2014) catalog (AB) or SDSS ModelMag photometric measurement
u_err	Error on <i>u</i> -band magnitude from coadded Jiang et al. (2014) catalog or SDSS ModelMagErr value from SDSS pipeline
g_mag	SExtractor “AUTO” (i.e., Kron-line elliptical aperture) <i>g</i> -band magnitude from coadded Jiang et al. (2014) catalog (AB) or SDSS ModelMag photometric measurement
g_err	Error on <i>g</i> -band magnitude from coadded Jiang et al. (2014) catalog or SDSS ModelMagErr value from SDSS pipeline
r_mag	SExtractor “AUTO” (i.e., Kron-line elliptical aperture) <i>r</i> -band magnitude from coadded Jiang et al. (2014) catalog (AB) or SDSS ModelMag photometric measurement
r_err	Error on <i>r</i> -band magnitude from coadded Jiang et al. (2014) catalog or SDSS ModelMagErr value from SDSS pipeline
i_mag	SExtractor “AUTO” (i.e., Kron-line elliptical aperture) <i>i</i> -band magnitude from coadded Jiang et al. (2014) catalog (AB) or SDSS ModelMag photometric measurement
i_err	Error on <i>i</i> -band magnitude from coadded Jiang et al. (2014) catalog or SDSS ModelMagErr value from SDSS pipeline
z_mag	SExtractor “AUTO” (i.e., Kron-line elliptical aperture) <i>z</i> -band magnitude from coadded Jiang et al. (2014) catalog (AB) or SDSS ModelMag photometric measurement
z_err	Error on <i>z</i> -band magnitude from coadded Jiang et al. (2014) catalog or SDSS ModelMagErr value from SDSS pipeline
opt_src	Source of optical photometry. J14: coadded catalog of Jiang et al. (2014), SDSS: pipeline photometry from the single-epoch SDSS catalog
W1	WISE magnitude at 3.4 $\mu\text{m}$ measured with profile-fitting photometry (Vega). Only reported if W1 magnitude has an $S/N \geq 2$
W1sig	Uncertainty on W1 magnitude
W2	WISE magnitude at 4.6 $\mu\text{m}$ measured with profile-fitting photometry (Vega). Only reported if W2 magnitude has an $S/N \geq 2$
W2sig	Uncertainty on W2 magnitude
W3	WISE magnitude at 12 $\mu\text{m}$ measured with profile-fitting photometry (Vega). Only reported if W3 magnitude has an $S/N \geq 2$
W3sig	Uncertainty on W3 magnitude
W4	WISE magnitude at 22 $\mu\text{m}$ measured with profile-fitting photometry (Vega). Only reported if W4 magnitude has an $S/N \geq 2$

**Table 3**  
(Continued)

Column Name	Description
W4sig	Uncertainty on W4 magnitude
R-W1	$R - W1$ (Vega) color, useful to assess reddening of source
W1 - W2	WISE W1 - W2 color, which is used to determine whether the source is a WISE AGN
WISE_AGN_75	If WISE W1 - W2 color obeys the Assef et al. (2018) AGN selection at the 75% reliability threshold, this flag is set to “YES.” In the main body of the text, a source that meets this color criterion is considered a WISE AGN.
WISE_AGN_90	If WISE W1 - W2 color obeys the Assef et al. (2018) AGN selection at the 90% reliability threshold, this flag is set to “YES.”
Soft_flux	X-ray flux in the 0.5–2 keV band from LaMassa et al. (2016b)
Soft_DETML	Significance of X-ray detection in the soft band, where $det\_ml = -\ln P_{\text{random}}$ , with $P_{\text{random}}$ as the Poissonian probability that the detection is a random fluctuation
Soft_Lum	Log of the $k$ -corrected soft-band X-ray luminosity. Only computed if Soft_DETML > 10
Hard_flux	X-ray flux in the 2–10 (2–7) keV band for XMM-Newton (Chandra) sources from LaMassa et al. (2016b)
Hard_DETML	Significance of X-ray detection in the hard band, where $det\_ml = -\ln P_{\text{random}}$ , with $P_{\text{random}}$ as the Poissonian probability that the detection is a random fluctuation
Hard_Lum	Log of the $k$ -corrected hard-band X-ray luminosity. Only computed if Hard_DETML > 10
Full_flux	X-ray flux in the 0.5–10 (0.5–7) keV band for XMM-Newton (Chandra) sources from LaMassa et al. (2016b)
Full_DETML	Significance of X-ray detection in the full band, where $det\_ml = -\ln P_{\text{random}}$ , with $P_{\text{random}}$ as the Poissonian probability that the detection is a random fluctuation
Full_Lum	Log of the $k$ -corrected full-band X-ray luminosity. Only computed if Full_DETML > 10
Xray_Lum	Estimate of the $k$ -corrected 2–10 keV X-ray luminosity ( $L_X$ ). If Hard_DETML > 10, this value represents the measured $k$ -corrected hard X-ray luminosity. Otherwise, if Full_DETML > 10, the $k$ -corrected full-band luminosity is adjusted by a factor of 0.665 to convert to the 2–10 keV band luminosity. If both Hard_DETML and Full_DETML are below 10, the $k$ -corrected soft-band luminosity is scaled by a factor of 1.27 to convert to the 2–10 keV band luminosity.
Xray_AGN	If $L_X > 10^{42} \text{ erg s}^{-1}$ , the source is considered an X-ray AGN, and this flag is set to “YES.”
Log(N II_6584/ H_alpha)	Logarithm of the [N II] 6584 Å/H $\alpha$ ratio. Only populated for $z < 0.5$ sources spectroscopically identified as “Galaxies” in the SDSS pipeline with an S/N > 5 in the [N II] 6584 Å, [O III] 5007 Å, H $\alpha$ , and H $\beta$ lines. Emission line fluxes are measured by the SDSS pipeline.
Log(O III_5700/H_beta)	Logarithm of the [O III] 5007 Å/H $\alpha$ ratio. Only populated for $z < 0.5$ sources spectroscopically identified as “Galaxies” in the SDSS pipeline with an S/N > 5 in the [N II] 6584 Å, [O III] 5007 Å, H $\alpha$ , and H $\beta$ lines. Emission line fluxes are measured by the SDSS pipeline.
BPT Classification	BPT classification of sources at $z < 0.5$ that are classified as “Galaxies” in the SDSS pipeline, and with emission line fluxes significant at the $5\sigma$ level. “Sy2”: Seyfert 2 galaxy based on the definition of Kewley et al. (2001); “Comp”: Composite galaxy with emission line ratios between the theoretical starburst line of Kewley et al. (2001) and empirical dividing line of Kauffmann et al. (2003); “SF”: Star-forming galaxies with emission line ratios below the Kauffmann et al. (2003) demarcation.

**Note.** Table 3 is published in its entirety in the electronic edition of the *Astrophysical Journal*. A portion is shown here for guidance regarding its form and content.

for the 75% reliability selection. When commenting on demographics below, we consider any source that obeys the 75% reliability selection as a WISE AGN.

Finally, we include a column that indicates the reddening of the source by calculating the optical to MIR  $R - W1$  color (LaMassa et al. 2016a). We first convert the  $r$ -band magnitude in AB to  $R$  in Bessel using

$$R(\text{AB}) = r - 0.0576 - 0.3718 \times ((r - i) - 0.2589), \quad (2)$$

(Blanton et al. 2017), and then to Vega with

$$R(\text{Vega}) = R(\text{AB}) - 0.21. \quad (3)$$

As demonstrated in LaMassa et al. (2016a), obscured AGNs in the range  $0.5 < z < 1$  tend to have  $R - W > 4$  colors, which is a redshift regime where the traditional BPT diagnostic becomes untenable for observed-frame optical spectra.

We perform BPT analysis on the low-redshift sources ( $z < 0.5$ ) that are spectroscopically classified as “Galaxies” but have X-ray luminosities or  $W1 - W2$  colors consistent with AGNs and relevant emission line fluxes with an S/N > 5 (see below). Thus, we also report the ratios of [N II] 6584 Å/H $\alpha$  and [O III] 5007 Å/H $\beta$  and the BPT classifications in the published catalog, where applicable.

All catalog columns are summarized in Table 3.

## 5. Discussion

We report on the demographics of the AGNs in the spectroscopic sample, dividing AGNs based on their optical spectroscopic classifications:

1. “Type 1 AGNs” have at least one broad emission line in their SDSS spectra (i.e., labeled as “QSO” in the SDSS pipeline and Table 2);
2. “Optically obscured AGNs” have no broad lines (i.e., labeled as “Galaxy” in Table 2), but are AGNs on the basis of their X-ray luminosity or WISE colors.

We note that four objects from archival spectroscopic databases do not report optical classifications, so we do not include these sources when discussing Type 1 versus optically obscured AGNs. All four sources have extragalactic redshifts, one is an X-ray AGN, and one is a WISE AGN. In the Appendix, we discuss how the demographics of the Stripe 82 X-ray AGNs compare with the AGNs from the XMM-XXL Northern survey (Liu et al. 2016; Menzel et al. 2016; Pierre et al. 2016).

### 5.1. Demographics of X-Ray and WISE AGNs

Of the 4847 sources in our spectroscopic sample, 4782 are extragalactic and 65 are stars (46 X-ray-emitting stars and 19 stars with WISE  $W1 - W2$  colors that meet the AGN 75%



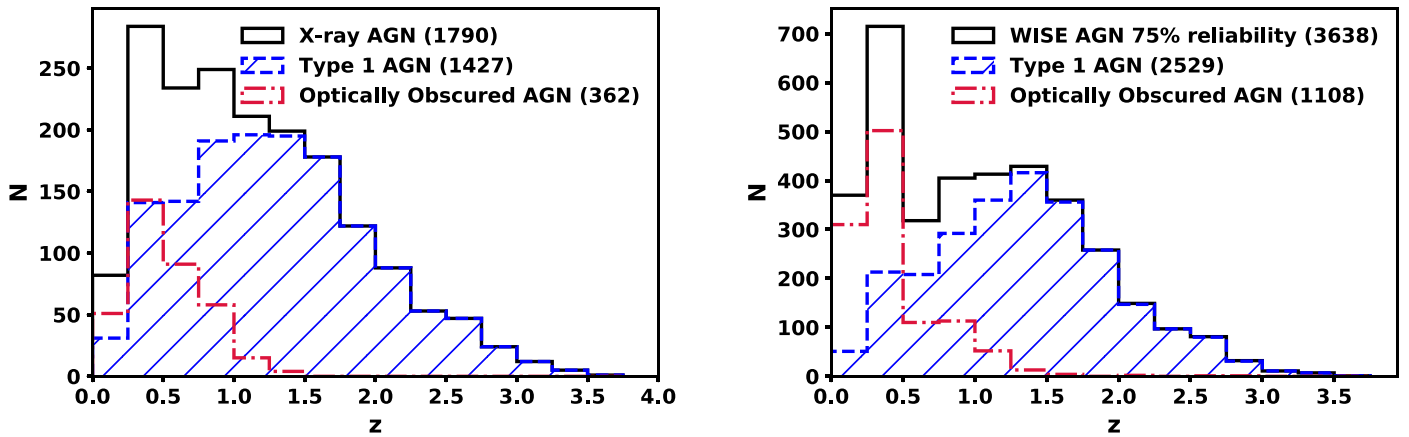


**Figure 12.** Redshift distribution of the (left) X-ray AGNs and (right) *WISE* AGNs; note that one X-ray and one *WISE* AGN included in the total sample lack spectroscopic classifications in archival catalogs and are thus not included in the Type 1 and optically obscured AGN subsamples. The subsets of sources that are Type 1 AGNs and optically obscured AGNs are shown by the dashed blue hatched histogram and the red dotted–dashed histogram, respectively. A prominent peak at  $z \sim 0.3$  is apparent in the *WISE* AGN optically obscured population. For both samples, the optically obscured AGNs are at lower redshift than the Type 1 AGNs. The median redshift of this sample of AGNs is  $z \sim 1$  for both the X-ray and *WISE* AGNs.

reliability threshold). Considering the extragalactic sample, we find 1790 X-ray AGNs (i.e.,  $L_X > 10^{42} \text{ erg s}^{-1}$ ), 3638 *WISE* AGNs, and 698 X-ray and *WISE* AGNs. Fifty-five sources are X-ray galaxies (i.e.,  $L_X < 10^{42} \text{ erg s}^{-1}$ ), but three of these are classified as AGNs based on their *WISE*  $W1 - W2$  colors.

In Table 4, we summarize the X-ray and *WISE* AGN classifications for the spectroscopic sample within the SDSS-IV eBOSS Stripe 82X field. Of the 4730 AGNs in the survey area, 70% are Type 1 and 30% are optically obscured. Because our sample is over 80% complete to  $r \sim 22$ , these demographics may be representative of the X-ray- and MIR-selected AGN population up to the optical, X-ray, and MIR flux limits of these surveys, but as we discuss further below, the total number of AGNs, and the number of optically obscured AGNs, may be biased by a significant fraction of star-forming galaxy interlopers with *WISE* AGN colors at  $z \sim 0.3$ . When considering the *WISE* and AGN samples separately, we do find a higher percentage of optically obscured *WISE* AGNs (30%) than X-ray AGNs (20%).

For reference, we include a demographic summary of the AGNs classified from the SDSS-IV eBOSS Stripe 82X survey in Table 4, highlighting that an overwhelming fraction of the optically obscured AGNs in the field (76%) were garnered from this dedicated follow-up program. These results underscore the importance of spending resources to follow up X-ray- and MIR-selected AGN candidates for a complete census of obscured black hole growth.

The AGNs span a redshift range of  $0.02 < z < 4.2$ , with a median redshift of  $z \sim 1$ , as shown in Figure 12. In the redshift distribution for the optically obscured *WISE* AGNs, a prominent peak is visible at  $z \sim 0.3$ . For both the X-ray and *WISE* AGNs, the Type 1 subpopulations are visible to a higher redshift than the optically obscured AGNs.

#### 5.1.1. BPT Analysis of Local Obscured AGNs

We perform BPT analysis for the subset of sources optically spectroscopically identified as “Galaxies” at  $z < 0.5$  that have a S/N of at least 5 in the  $H\alpha$ ,  $H\beta$ ,  $[O\text{ III}]$  5007 Å, and  $[N\text{ II}]$  6584 Å lines. Here, we use the Kewley et al. (2001) maximal starburst line to define Seyfert 2 galaxies, and the empirical Kauffmann et al. (2003) demarcation to separate star-forming

**Table 4**  
Demographic Summary of Stripe 82X Sources in SDSS-IV eBOSS Survey Area<sup>a</sup>

Classification	X-ray AGNs <sup>b</sup>	<i>WISE</i> AGNs	X-ray and <i>WISE</i> AGNs	Total X-ray or <i>WISE</i> AGNs
Total				
Type 1 AGNs	1427	2529	646	3310
Optically obscured AGNs	362	1108	52	1418
Stars	46	19	0	65
SDSS-IV eBOSS Sources				
Type 1 AGNs	335	354	85	604
Optically obscured AGNs	269	844	40	1073
Stars	27	13	0	40

#### Notes.

<sup>a</sup> X-ray sources are mostly within the  $15.6 \text{ deg}^2$  footprint of the *XMM-Newton* AO13 survey, while *WISE* sources are from the larger  $36.8 \text{ deg}^2$  footprint of the SDSS-IV eBOSS Stripe 82X spectroscopic survey. We note that one X-ray AGN and one *WISE* AGN do not have spectroscopic classifications in archival databases and are thus not included in the Type 1 and optically obscured AGN census above.

<sup>b</sup> X-ray sources where  $L_X > 10^{42} \text{ erg s}^{-1}$  and are thus classifiable as AGNs based on their powerful X-ray emission. We list the number of X-ray-detected stars (and stars with *WISE*  $W1 - W2$  colors consistent with AGNs) for reference. In addition to the sources listed here, there are 55 X-ray galaxies (i.e., X-ray sources with  $L_X < 10^{42} \text{ erg s}^{-1}$ ), three of which are classified as AGNs based on their *WISE* colors; six of these X-ray galaxies are from the eBOSS survey.

galaxies from composite galaxies, which have a mixture of star-forming and AGN ionization powering their emission.

For the X-ray AGNs (left panel of Figure 13), we see that 18% of the sources (14 out of 76) would be misclassified as non-AGNs on the basis of their optical emission alone. However, based on their X-ray luminosities, these galaxies do host active central black holes. Similar results, that is, X-ray AGNs hosted in BPT-classified star-forming galaxies, have been observed in other X-ray samples (so-called “optically elusive AGNs”; Maiolino et al. 2003; Caccianiga et al. 2007; Pons & Watson 2014; Smith et al. 2014; Menzel et al. 2016).

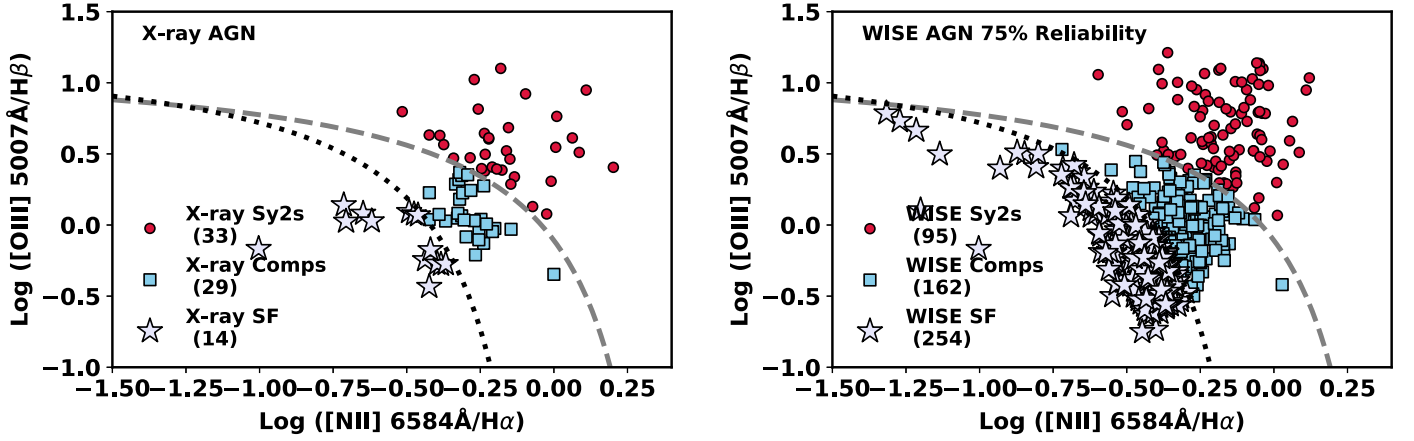


**Figure 13.** BPT diagram for the  $z < 0.5$  (left) X-ray AGNs and (right) *WISE* AGNs at the 75% reliability level that are spectroscopically identified as “Galaxies” and have an S/N exceeding 5 in the  $H\alpha$ ,  $H\beta$ ,  $[O\text{ III}]$  5007 Å, and  $[N\text{ II}]$  6584 Å emission lines; fluxes are derived from the SDSS pipeline fit to the spectra. The gray dashed line notes the maximal starburst line from Kewley et al. (2001) where the emission line ratios indicate AGN ionization, and the black dotted line notes the empirical dividing line between star-forming and composite galaxies from Kauffmann et al. (2003). About one-fifth of the X-ray AGNs would be missed based on optical characteristics, while half of the *WISE* AGNs are spectroscopically identified as star-forming galaxies. Whether this latter class represents elusive AGNs whose optical signatures are buried by dust or star-forming galaxies whose MIR colors mimic those of AGNs is unclear.

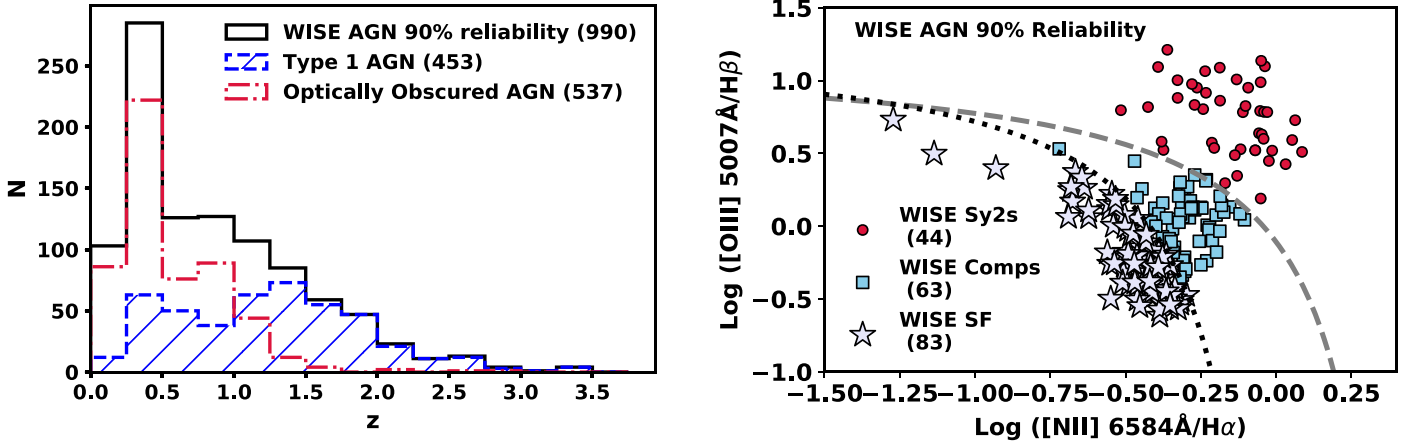


**Figure 14.** (Left): redshift distribution and (right) BPT diagram of *WISE* AGNs identified at the 90% reliability level (Assef et al. 2018). The prominent peak at  $z \sim 0.3$  and relatively high percentage of *WISE* AGNs spectroscopically classified as star-forming galaxies remain, indicating that more stringent MIR color cuts do not erase the trends observed at the 75% reliability level. Theoretical modeling would be needed to test whether the *WISE* AGN color selection fails at  $z \sim 0.3$ , preferentially selecting nonactive galaxies, or if this population represents a new class of buried AGNs.

A much higher percentage (50%) of *WISE* AGNs at  $z < 0.5$  are classified as star-forming galaxies (right panel of Figure 13). The nature of these objects is less clear than for the X-ray AGNs. Combined with the redshift peak of *WISE* AGNs at  $z \sim 0.3$ , these results may point to a degeneracy in *WISE* AGN color selection, where star-forming galaxies at these redshifts can have MIR colors mimicking AGNs (see Satyapal et al. 2018). If we restrict the *WISE* AGNs to those defined at the 90% reliability level of Assef et al. (2018), we see a similar trend: a peak in the AGN distribution at  $z \sim 0.3$  remains (Figure 14, left), and the fraction of *WISE* AGNs in the star-forming locus of the BPT diagram is similar (44%, Figure 14, right). Distinguishing between optically buried AGNs and star-forming galaxy impostors masquerading as MIR AGNs at  $z \sim 0.3$  would require further theoretical modeling (Satyapal et al. 2018), which will be the topic of a future paper.

## 5.2. Comparison between X-Ray and *WISE* AGNs

Here we explore the characteristics of AGNs found, and missed, by X-ray and MIR selection. We reiterate that the area of the SDSS plates in the eBOSS program is larger than the field of view of the *XMM-Newton* AO13 observations in Stripe 82 (Figure 2). Thus, for the most straightforward comparison between the demographics of the X-ray and *WISE* AGNs, we cull the *WISE* list to only include those sources detected within the 15.6 deg<sup>2</sup> footprint of the *XMM-Newton* AO13 Stripe 82 survey area; we also remove the archival X-ray sources from the eBOSS program that do not overlap the AO13 survey area. Table 5 provides a demographic summary of the X-ray and *WISE* sources used in this analysis, amounting to 2751 AGNs total.

We immediately see from Table 5 that the space density is comparable between the *WISE* AGNs ( $\sim 108/\text{deg}^2$ ) and the X-ray AGNs ( $\sim 114/\text{deg}^2$ ). Only  $\sim 23\%$  of the X-ray or *WISE*

**Table 5**  
Classification Summary of Sources That Overlap the 15.6 deg<sup>2</sup> *XMM-Newton* AO13 Footprint<sup>a</sup>

Classification	X-ray AGNs	WISE AGNs	X-ray and WISE AGNs	X-ray or WISE AGNs
Type 1 AGNs	1413	1172	639	1946
Optically obscured AGNs	361	495	52	804

**Note.**

<sup>a</sup> There is an additional X-ray AGN that lacks an optical spectroscopic classification in the archival catalogs.

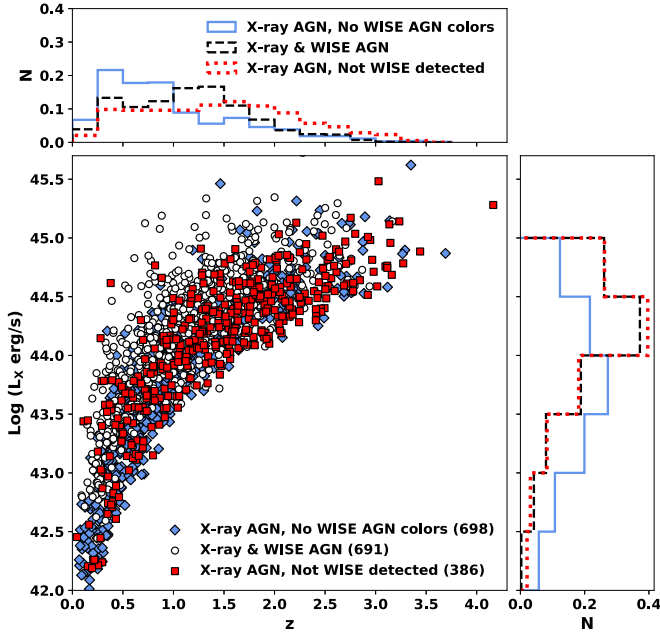


**Figure 15.** X-ray luminosity as a function of redshift for X-ray AGNs that are detected by *WISE* and have  $W1 - W2$  colors bluer than the Assef et al. (2018) 75% reliability color cut (blue diamonds; solid blue histogram), have  $W1 - W2$  colors that obey the Assef et al. (2018) color criterion (white circles; black dashed histogram), and those undetected by *WISE* (red squares; red dotted histogram). The X-ray AGNs with blue *WISE* colors tend to have moderate X-ray luminosities (i.e.,  $10^{42.5} < L_X < 10^{44}$  erg s<sup>-1</sup>) and lie below  $z < 1$ , while those undetected by *WISE* populate the same parameter space as those with *WISE* AGN colors: a not-insignificant fraction of luminous black hole growth is missed by  $W1 - W2$  selection, due to *WISE* nondetections. Normalized histograms are shown to better illustrate the parameter space spanned by these source populations.

AGNs in this sample are classified as AGNs on the basis of optical broad lines, X-ray luminosity, and MIR colors (639 out of 2751). Of the 804 obscured AGNs, only ~6% are identified as accreting black holes on the basis of both X-ray emission and red MIR colors.

In Figures 15 and 16, we explore the populations detected and missed by defining AGNs based on X-ray luminosity and MIR color, highlighting the complementarity of multiple selection criteria to offer a comprehensive view of black hole growth.

The 1775 X-ray AGNs are shown in Figure 15, where we highlight the subset of sources also identified as AGNs on the basis of their  $W1 - W2$  colors (691; 39%), those AGNs detected by *WISE* but with bluer  $W1 - W2$  colors than the Assef et al. (2018) 75% reliability color cut (698; 39%), and those undetected by *WISE* (386; 22%). Similar to trends previously reported in other samples (e.g., Eckart et al. 2010; Mendez et al. 2013; LaMassa et al. 2016a; Menzel et al. 2016), the X-ray AGNs detected by *WISE* that do not meet the  $W1 - W2$  color criterion tend to be at low to moderate X-ray

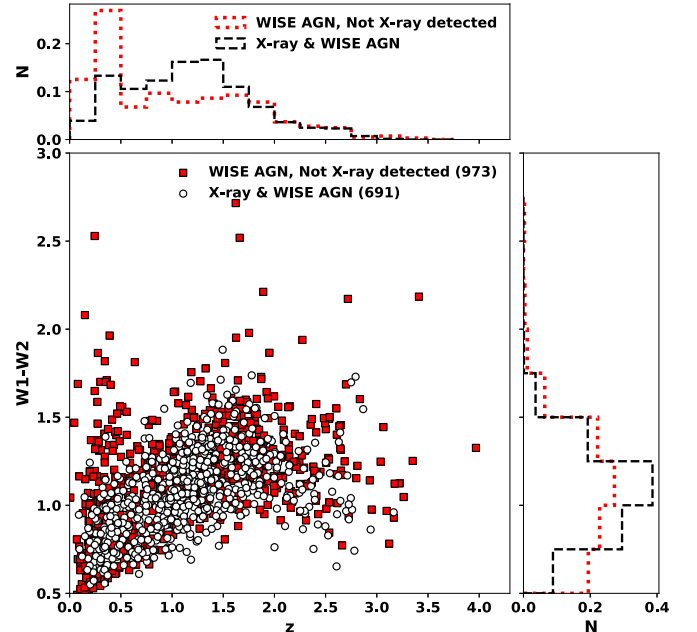


**Figure 16.** MIR  $W1 - W2$  color as a function of redshift for the *WISE* AGNs, with those sources also identified as AGNs by their X-ray luminosity (white circles; black dashed histogram) and those completely undetected in X-rays (red squares; red dotted histogram) shown; not shown are the three X-ray sources with X-ray luminosities below  $10^{42}$  erg s<sup>-1</sup>. Of the *WISE* AGNs, 58% are not detected in X-rays. No  $W1 - W2$  color trend is seen between X-ray detections and nondetections, as would be expected if the *WISE* AGNs not detected in X-rays were more obscured. Normalized histograms are shown to better illustrate the parameter space spanned by these source populations.

luminosities (i.e., 64% have  $L_X < 10^{44}$  erg s<sup>-1</sup>). This percentage is consistent with the 50%–70% of X-ray AGNs not identified as such by their  $W1 - W2$  colors found by Georgakakis et al. (2017), albeit with a more conservative color cut ( $W1 - W2 > 0.8$ ) than what we use here. It is reasonable to assume that in these cases, the AGN is not dominating the MIR emission, which is a population to which the  $W1 - W2$  color selection is not tuned.

However, we also find that though MIR-selected AGNs are found at the highest X-ray luminosities and redshifts, the X-ray sources *undetected* by *WISE* populate the same parameter space. About one-third of the highest luminosity ( $L_X > 10^{44}$  erg s<sup>-1</sup>), highest redshift ( $z > 1$ ) X-ray AGNs are undetected by *WISE*, indicating that MIR selection can miss a nonnegligible fraction of the most luminous black hole growth. Many of these sources may be “hot dust poor quasars” described in Hao et al. (2010, 2011) and Lyu et al. (2017). This population was shown to have anomalously weak rest-frame NIR emission between 1 and 3  $\mu$ m compared to other Type 1 AGNs, which can be explained by a low dust covering factor. Indeed, the rest-frame  $W1$  and  $W2$  passbands at  $z > 1$  probe rest-frame NIR emission, suggesting this interpretation has

some merit. However, fitting the broadband SEDs of these sources to derive NIR and optical slopes is required to test whether they fit the definition of “hot dust poor quasars,” which will be explored in a follow-up paper.

We perform the corollary analysis in Figure 16, where we investigate the  $W1 - W2$  color as a function of redshift for the 691 *WISE* and X-ray AGNs and the 973 *WISE* AGNs not detected in X-rays (only three sources classified as *WISE* AGNs are X-ray galaxies), representing 42% and 58% of the *WISE* AGNs, respectively. Though it seems plausible that the *WISE* AGNs undetected by X-rays suffer from high levels of extinction, we do not observe that these sources have redder  $W1 - W2$  colors than the X-ray-detected AGNs.

## 6. Conclusions

We reported on the results of an SDSS-IV eBOSS spectroscopic survey that covered  $36.8 \text{ deg}^2$  of Stripe 82 in the fall of 2015. About half of this survey area ( $15.6 \text{ deg}^2$ ) overlaps the largest contiguous region of the Stripe 82 X-ray survey observed by *XMM-Newton* in AO13 (PI: Urry; LaMassa et al. 2016b). The primary targets of this survey were X-ray sources and *WISE* AGN candidates from the ALLWISE survey (Mainzer et al. 2011) identified on the basis of their  $W1 - W2$  colors (i.e., the 75% reliability threshold of Assef et al. 2013). SDSS counterparts to the X-ray and *WISE* sources were identified using the statistical maximum likelihood approach, as described in LaMassa et al. (2016b) for the X-ray sources and in the main text for the *WISE* population. Additional “filler” targets were observed to make use of all available spectroscopic fibers across the SDSS plates. Subsequent to the SDSS-IV eBOSS observing program, an updated multiwavelength catalog matched to the Stripe 82X survey was published by Ananna et al. (2017), and the  $W1 - W2$  color criteria for AGNs were modified with respect to the eBOSS target list we created (Assef et al. 2018), leading us to curate the sources in our final published catalog with respect to the objects we targeted.

In total, 2262 SDSS counterparts to the original X-ray and *WISE* AGN candidate target lists were spectroscopically observed. We visually inspected all spectra, finding that 1769 sources (78%) were of sufficient quality to determine redshifts and classifications, where we achieved a  $\sim 37\%$  identification rate at the faintest magnitudes ( $22.5 < r < 23.5$ ; Figure 8). We recommend visual inspection of spectra flagged by ZWARNING or having  $S/N < 2.25$  to maximize sample size and reliability of results; only 3% of sources not flagged by ZWARNING and with  $S/N > 2.25$  were found to have discrepant redshifts or classifications between visual inspection and the pipeline. If limited resources preclude visual inspection of spectra, then imposing an  $S/N$  threshold exceeding 2.25 and a null ZWARNING flag would result in a reliable sample, but at the expense of discarding  $\sim 30\%$  of spectra that would otherwise be of sufficient quality for analyzing source demographics.

After vetting the SDSS spectroscopic results and curating the target lists to only include X-ray/SDSS counterparts from Ananna et al. (2017) and *WISE* AGNs meeting the Assef et al. (2018)  $W1 - W2$  color criteria at the 75% level, we combined this sample with X-ray and *WISE* AGNs in the survey area with spectroscopic redshifts from other SDSS programs (Abazajian et al. 2009; Aihara et al. 2011; Alam et al. 2015; Albareti et al. 2017; P  ris et al. 2017, 2018; Abolfathi et al. 2018), 2SLAQ (Croom et al. 2009), 6dF (Jones et al. 2004, 2009), and dedicated follow-up programs of Stripe 82 X-ray sources

(LaMassa et al. 2016b, 2017). The total sample is 82% complete to  $r \sim 22$ , with the X-ray and *WISE* AGN samples being  $\sim 88\%$  and  $\sim 82\%$  complete at this magnitude limit (Figure 11).

Our spectroscopic sample consists of 4847 sources, of which 4730 are AGNs (1790 X-ray AGNs, 3638 *WISE* AGNs, 698 X-ray and *WISE* AGNs): 3310 are Type 1 AGNs (70%) and 1418 are optically obscured AGNs (30%; Table 4); two AGNs did not have spectroscopic classifications in the archival catalogs we queried. A vast majority of the optically obscured AGNs (76%) were identified via the eBOSS Stripe 82X survey. The AGNs range in redshift over  $0.02 < z < 4.2$ , with a median redshift of  $z \sim 1$  (Figure 12). BPT analysis of the  $z < 0.5$  AGNs with high-S/N emission lines shows that 50% of the *WISE* AGNs occupy the star-forming locus (Figure 13); whether these sources are optically buried AGNs or star-forming galaxies whose MIR colors mimic those of AGNs requires further analysis (e.g., Satyapal et al. 2018).

In the  $15.6 \text{ deg}^2$  area of the *XMM-Newton* AO13 Stripe 82 footprint, we compared the AGN populations from X-ray and MIR selection (Table 5), finding the following trends among the 2751 AGNs in this area-restricted sample:

1. Only  $\sim 6\%$  of the optically obscured AGNs (52 out of 804) are both X-ray and *WISE* AGNs, highlighting the importance of both X-ray and MIR selection to recover AGNs missed by optical surveys;
2. 61% of X-ray AGNs (1084 out of 1775) are not MIR AGNs (Figure 15):
  - (a) 39% are detected by *WISE* but have  $W1 - W2$  colors too blue for the Assef et al. (2018) 75% reliability color definition. These sources are generally at lower luminosity, where the AGN is not contributing significantly to the MIR SED (see also, e.g., Eckart et al. 2010; Mendez et al. 2013; Menzel et al. 2016; LaMassa et al. 2016a).
  - (b) 22% are *undetected* by *WISE*. These sources are generally X-ray luminous (i.e.,  $L_x > 10^{44} \text{ erg s}^{-1}$ ), challenging the conventional wisdom that MIR color selection identifies all luminous AGNs: these sources may have anomalous dust properties, similar to “hot dust poor” or “hot dust deficient” quasars (Hao et al. 2010, 2011; Lyu et al. 2017).
3. 58% of *WISE* AGNs (973 out of 1664) are not detected in X-rays (Figure 16), but there is no clear  $W1 - W2$  color difference between X-ray AGNs and nondetections, indicating that the *WISE* AGNs undetected in X-rays are not redder and hence may not preferentially be more obscured.

We thank the referee for a careful reading of the manuscript and for providing insightful comments that helped us streamline the paper.

Funding for the Sloan Digital Sky Survey IV has been provided by the Alfred P. Sloan Foundation, the U.S. Department of Energy Office of Science, and the Participating Institutions. SDSS-IV acknowledges support and resources from the Center for High-Performance Computing at the University of Utah. The SDSS website is [www.sdss.org](http://www.sdss.org).

SDSS-IV is managed by the Astrophysical Research Consortium for the Participating Institutions of the SDSS Collaboration, including the Brazilian Participation Group, the Carnegie Institution for Science, Carnegie Mellon University,



the Chilean Participation Group, the French Participation Group, Harvard-Smithsonian Center for Astrophysics, Instituto de Astrofísica de Canarias, The Johns Hopkins University, Kavli Institute for the Physics and Mathematics of the Universe (IPMU)/University of Tokyo, Lawrence Berkeley National Laboratory, Leibniz Institut für Astrophysik Potsdam (AIP), Max-Planck-Institut für Astronomie (MPIA Heidelberg), Max-Planck-Institut für Astrophysik (MPA Garching), Max-Planck-Institut für Extraterrestrische Physik (MPE), National Astronomical Observatories of China, New Mexico State University, New York University, University of Notre Dame, Observatório Nacional/MCTI, The Ohio State University, Pennsylvania State University, Shanghai Astronomical Observatory, United Kingdom Participation Group, Universidad Nacional Autónoma de México, University of Arizona, University of Colorado Boulder, University of Oxford, University of Portsmouth, University of Utah, University of Virginia, University of Washington, University of Wisconsin, Vanderbilt University, and Yale University.

This research made use of Astropy, a community-developed core Python package for Astronomy (The Astropy Collaboration et al. 2018).

Some of the data presented herein were obtained at the W. M. Keck Observatory, which is operated as a scientific partnership among the California Institute of Technology, the University of California, and the National Aeronautics and Space Administration. The Observatory was made possible by the generous financial support of the W. M. Keck Foundation. The authors wish to recognize and acknowledge the very significant cultural role and reverence that the summit of Maunakea has always had within the indigenous Hawaiian community. We are most fortunate to have the opportunity to conduct observations from this mountain.

S.M.L. acknowledges funding support from 17-ADAP17-0055.

*Facilities:* Sloan, XMM, CXO, Hale, WIYN, Keck:I (LRIS), Gemini:Gillet.

## Appendix Comparison between Stripe 82X AGNs and XMM-XXL-N AGNs

We compare the X-ray AGNs identified in this program with those observed in a similar SDSS BOSS program to target X-ray AGNs from the 18 deg<sup>2</sup> XMM-XXL northern field (Menzel et al. 2016). With a flux limit of  $\sim 3.5 \times 10^{-15}$  erg s<sup>-1</sup> cm<sup>-2</sup> at 50% of the survey area, it is slightly more sensitive than the *XMM-Newton* AO13 component of the Stripe 82X survey ( $F_{0.5-2 \text{ keV, lim}} \sim 5 \times 10^{-15}$  erg s<sup>-1</sup> cm<sup>-2</sup> at half the survey area). Out of 8445

X-ray point sources in the XMM-XXL-N field (Liu et al. 2016; Pierre et al. 2016), 3004 were spectroscopically followed up by BOSS, garnering reliable redshifts and spectroscopic classifications for 2514 extragalactic sources (including two blazars) and 85 stars. We a priori remove the 57 sources with “not classifiable” BOSS spectra from the Menzel et al. (2016) catalog in our comparison below, since though their redshifts are securely determined via visual inspection, the low S/N of the spectra precludes optical spectroscopic classification.

We follow our categorization scheme above when classifying the sources in Menzel et al. (2016), where the optical spectroscopic classification of “Type 1 AGN” refers to objects that have at least one broad emission line and “Optically Obscured AGN” indicates sources with narrow emission lines only or absorption lines, regardless of their BPT designation. We consider these objects X-ray AGNs if their estimated  $k$ -corrected 2–10 keV luminosity ( $L_X$ ) exceeds  $10^{42}$  erg s<sup>-1</sup>, where we follow a prescription similar to that of the Stripe 82X sources to calculate  $L_X$  if the source is not detected in the hard band. Here, we use  $\Gamma = 1.4$  to calculate  $k$ -corrected luminosities because this was the spectral slope assumed by Liu et al. (2016) when converting from counts to fluxes. Based on this spectral slope, we use a correction factor of 0.74 and 2.88 to convert the luminosity from the 0.5 to 10 keV and 0.5 to 2 keV bands, respectively, to the 2–10 keV band.

In XMM-XXL-N, we find 1787 Type 1 AGNs and 654 optically obscured AGNs. The detection threshold for the XMM-XXL-N sources in Liu et al. (2016) is lower than that used in Stripe 82X, with a detection significance set to  $P < 4 \times 10^{-6}$  for XMM-XXL-N, compared with  $P < 3 \times 10^{-7}$  for Stripe 82X. Due to the lower significance threshold of XMM-XXL-N and the deeper observations, the number density of spectroscopically confirmed X-ray AGNs in the 18 deg<sup>2</sup> XMM-XXL-N ( $\sim 136$  deg<sup>-2</sup>) is higher than that of the 15.6 deg<sup>2</sup> Stripe 82X XMM-AO13 field ( $\sim 114$  deg<sup>2</sup>).

We find a smaller fraction of optically obscured X-ray AGNs between Stripe 82X (20%) compared with XMM-XXL-N (27%). However, despite the higher number density of AGNs in XMM-XXL-N, the number of high-redshift ( $z > 2.5$  for Type 1 AGNs;  $z > 0.75$  for optically obscured AGNs) and high-luminosity ( $L_X > 10^{44.5}$  erg s<sup>-1</sup> for Type 1 AGNs;  $L_X > 10^{43.5}$  erg s<sup>-1</sup> for optically obscured AGNs) are similar, as demonstrated in Figure 17. Hence, a wide area at moderate depths ( $\sim 5 \times 10^{-15}$  erg s<sup>-1</sup> cm<sup>-2</sup>) is more important than deeper coverage in unveiling AGNs at the highest luminosities and redshifts.

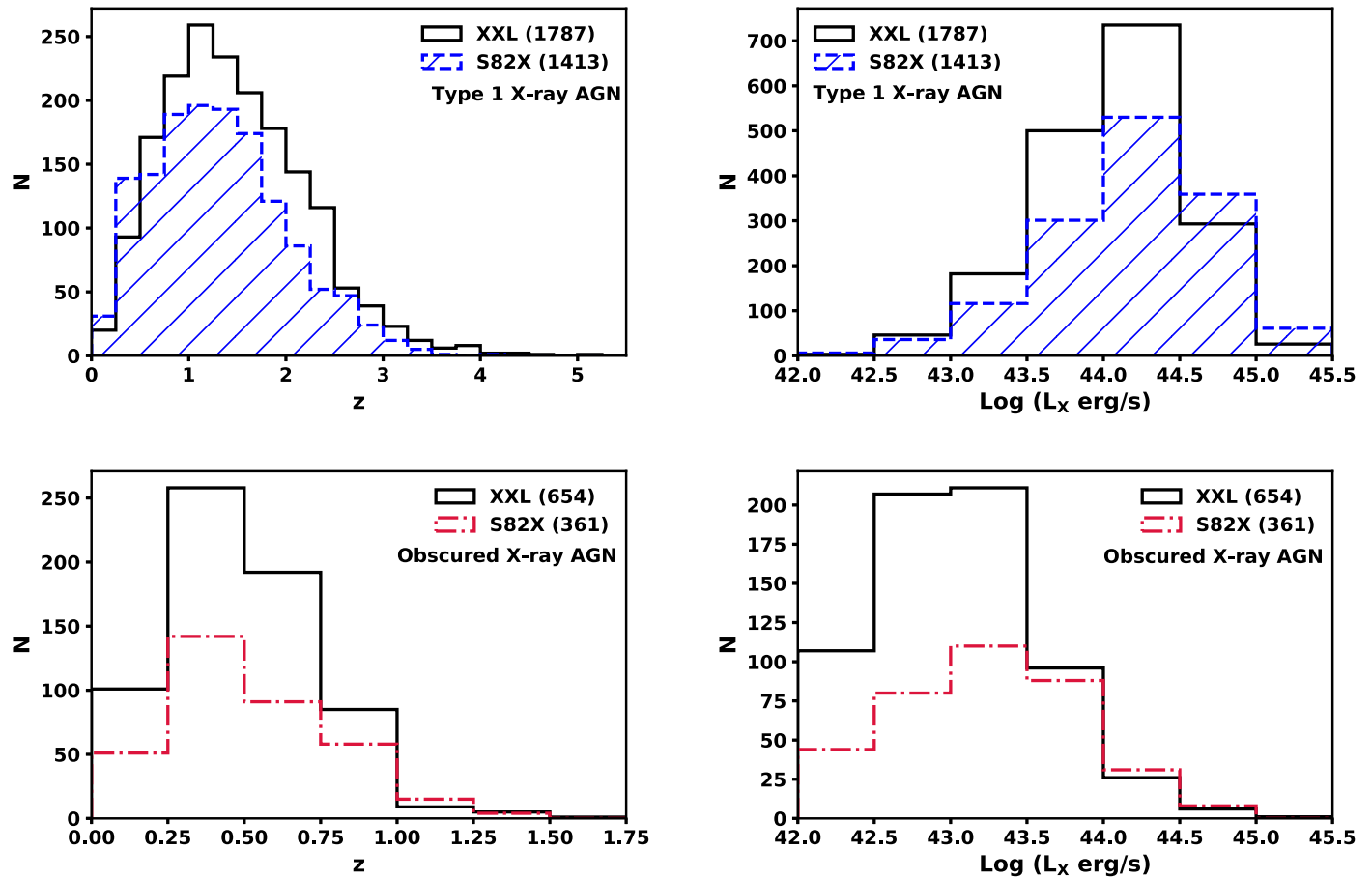


**Figure 17.** (Left): redshift and (right) X-ray luminosity distribution for (top) Type 1 and (bottom) optically obscured X-ray AGNs from the 18  $\text{deg}^2$  XMM-XXL-N survey (black solid line; Liu et al. 2016; Menzel et al. 2016; Pierre et al. 2016) and the 15.6  $\text{deg}^2$  XMM-Newton AO13 portion of the Stripe 82X survey (blue hatched histogram for Type 1 AGNs; red dotted-dashed histogram for optically obscured AGNs). Though XMM-XXL-N has a higher number density of AGNs due to deeper coverage and a lower detection threshold, the numbers of AGNs detected at the highest redshifts and luminosities are comparable between the two surveys, demonstrating the necessity of wide areal coverage to build statistics in this parameter space.

### ORCID iDs

Stephanie M. LaMassa <https://orcid.org/0000-0002-5907-3330>  
Mara Salvato <https://orcid.org/0000-0001-7116-9303>  
Tonima Tasnim Ananna <https://orcid.org/0000-0001-8211-3807>  
C. Meg Urry <https://orcid.org/0000-0002-0745-9792>  
Nicholas Ross <https://orcid.org/0000-0003-1830-6473>

### References

- Abazajian, K. N., Adelman-McCarthy, J. K., Agüeros, M. A., et al. 2009, *ApJS*, **182**, 543
- Abolfathi, B., Aguado, D. S., Aguilar, G., et al. 2018, *ApJS*, **235**, 42
- Aihara, H., Allende Prieto, C., An, D., et al. 2011, *ApJ*, **193**, 29
- Alam, S., Albareti, F. D., Allende Prieto, C., et al. 2015, *ApJS*, **219**, 12
- Albareti, F. D., Allende Prieto, C., Almeida, A., et al. 2017, *ApJS*, **233**, 25
- Alexander, D. M., Bauer, F. E., Brandt, W. N., et al. 2003, *AJ*, **126**, 539
- AlSaiyad, Y., McGreer, I. D., Fan, X., et al. 2015, AAS Meeting, **225**, 144.46
- Ananna, T. T., Salvato, M., LaMassa, S., et al. 2017, *ApJ*, **850**, 66
- Annis, J., Soares-Santos, M., Strauss, M. A., et al. 2014, *ApJ*, **794**, 120
- Assef, R. J., Stern, D., Kochanek, C. S., et al. 2013, *ApJ*, **772**, 26
- Assef, R. J., Stern, D., Noirot, G., et al. 2018, *ApJS*, **234**, 23
- Baldwin, J. A., Phillips, M. M., & Terlevich, R. 1981, *PASP*, **93**, 5
- Barmby, P., Alonso-Herrero, A., Donley, J. L., et al. 2006, *ApJ*, **642**, 126
- Bassani, L., Dadina, M., Maiolino, R., et al. 1999, *ApJS*, **121**, 473
- Becker, R. H., White, R. L., & Helfand, D. J. 1995, *ApJ*, **450**, 559
- Blanton, M. R., Bershad, M. A., Abolfathi, B., et al. 2017, *AJ*, **154**, 28
- Bolton, A. S., Schlegel, D. J., Aubourg, É., et al. 2012, *AJ*, **144**, 144
- Brandt, W. N., & Alexander, D. M. 2015, *A&ARv*, **23**, 1
- Brandt, W. N., & Hasinger, G. 2005, *ARA&A*, **43**, 827
- Brusa, M., Civano, F., Comastri, A., et al. 2010, *ApJ*, **716**, 348
- Brusa, M., Zamorani, G., Comastri, A., et al. 2007, *ApJS*, **172**, 353
- Caccianiga, A., Severgnini, P., Della Ceca, R., et al. 2007, *A&A*, **470**, 557
- Cappelluti, N., Brusa, M., Hasinger, G., et al. 2009, *A&A*, **497**, 635
- Cardamone, C. N., Urry, C. M., Damen, M., et al. 2008, *ApJ*, **680**, 130
- Casali, M., Adamson, A., Alves de Oliveira, C., et al. 2017, *A&A*, **467**, 777
- Civano, F., Elvis, M., Brusa, M., et al. 2012, *ApJS*, **201**, 30
- Civano, F., Marchesi, S., Comastri, A., et al. 2016, *ApJ*, **819**, 62
- Comastri, A., Ranalli, P., Iwasawa, K., et al. 2011, *A&A*, **526**, L9
- Croom, S. M., Richards, G. T., Shanks, T., et al. 2009, *MNRAS*, **392**, 19
- Dawson, K. S., Kneib, J.-P., Percival, W. J., et al. 2016, *AJ*, **151**, 44
- Delubac, T., Raichoor, A., Comparat, J., et al. 2017, *MNRAS*, **465**, 1831
- Denney, K. D., De Rosa, G., Croxall, K., et al. 2014, *ApJ*, **796**, 134
- DiPompeo, M. A., Myers, A. D., Hickox, R. C., Geach, J. E., & Hainline, K. N. 2014, *MNRAS*, **442**, 3443
- Donley, J. L., Koekemoer, A. M., Brusa, M., et al. 2012, *ApJ*, **748**, 142
- Dwelly, T., Salvato, M., Merloni, A., et al. 2017, *MNRAS*, **469**, 1065
- Eckart, M. E., McGreer, I. D., Stern, D., Harrison, F. A., & Helfand, D. J. 2010, *ApJ*, **708**, 584
- Elvis, M., Civano, F., Vignali, C., et al. 2009, *ApJS*, **184**, 158
- Fiore, F., La Franca, F., Vignali, C., et al. 2000, *NewA*, **5**, 143
- Fliri, J., & Trujillo, I. 2016, *MNRAS*, **456**, 1359
- Frieman, J. A., Bassett, B., Becker, A., et al. 2008, *AJ*, **135**, 338
- Georgakakis, A., Salvato, M., Liu, Z., et al. 2017, *MNRAS*, **469**, 3232
- Gezari, S., Hung, T., Cenko, S. B., et al. 2017, *ApJ*, **835**, 144
- Giavalisco, M., Ferguson, H. C., Koekemoer, A. M., et al. 2004, *ApJL*, **600**, L93
- Gunn, J. E., Siegmund, W. A., Mannery, E. J., et al. 2006, *AJ*, **131**, 2332

- Hao, H., Elvis, M., Civano, F., et al. 2010, [ApJL](#), **724**, L59
- Hao, H., Elvis, M., Civano, F., & Lawrence, A. 2011, [ApJ](#), **733**, 108
- Hasinger, G., Cappelluti, N., Brunner, H., et al. 2007, [ApJS](#), **172**, 29
- Heckman, T. M., Ptak, A., Hornschemeier, A., & Kauffmann, G. 2005, [ApJ](#), **634**, 161
- Helfand, D. J., White, R. L., & Becker, R. H. 2015, [ApJ](#), **801**, 26
- Hewett, P. C., Warren, S. J., Leggett, S. K., & Hodgkin, S. T. 2006, [MNRAS](#), **367**, 454
- Hopkins, P. F., Hernquist, L., Cox, T. J., & Kereš, D. 2008, [ApJS](#), **175**, 356
- Jannuzi, B. T., & Dey, A. 1999, in ASP Conf. Ser. 193, The Hy-Redshift Universe: Galaxy Formation and Evolution at High Redshift, ed. A. J. Bunker & W. J. M. van Breugel (San Francisco, CA: ASP), 258
- Jiang, L., Fan, X., Bian, F., et al. 2014, [ApJS](#), **213**, 12
- Jones, D. H., Read, M. A., Saunders, W., et al. 2009, [MNRAS](#), **399**, 683
- Jones, D. H., Saunders, W., Colless, M., et al. 2004, [MNRAS](#), **355**, 747
- Juneau, S., Dickinson, M., Alexander, D. M., & Salim, S. 2011, [ApJ](#), **736**, 104
- Kauffmann, G., Heckman, T. M., Tremonti, C., et al. 2003, [MNRAS](#), **346**, 1055
- Kewley, L. J., Dopita, M. A., Leitherer, C., et al. 2013a, [ApJ](#), **774**, 100
- Kewley, L. J., Dopita, M. A., Sutherland, R. S., Heisler, C. A., & Trevena, J. 2001, [ApJ](#), **556**, 121
- Kewley, L. J., Maier, C., Yabe, K., et al. 2013b, [ApJL](#), **774**, L10
- Lacy, M., Storrie-Lombardi, L. J., Sajina, A., et al. 2004, [ApJS](#), **154**, 166
- Lamareille, F. 2010, [A&A](#), **509**, A53
- LaMassa, S. M., Cales, S., Moran, E. C., et al. 2015, [ApJ](#), **800**, 144
- LaMassa, S. M., Civano, F., Brusa, M., et al. 2016a, [ApJ](#), **818**, 88
- LaMassa, S. M., Glikman, E., Brusa, M., et al. 2017, [ApJ](#), **847**, 100
- LaMassa, S. M., Heckman, T. M., Ptak, A., et al. 2009, [ApJ](#), **705**, 568
- LaMassa, S. M., Heckman, T. M., Ptak, A., et al. 2011, [ApJ](#), **729**, 52
- LaMassa, S. M., Urry, C. M., Cappelluti, N., et al. 2013a, [MNRAS](#), **436**, 3581
- LaMassa, S. M., Urry, C. M., Cappelluti, N., et al. 2016b, [ApJ](#), **817**, 172
- LaMassa, S. M., Urry, C. M., Glikman, E., et al. 2013b, [MNRAS](#), **432**, 1351
- Lang, D., Hogg, D. W., & Schlegel, D. J. 2016, [AJ](#), **151**, 36
- Lansbury, G. B., Alexander, D. M., Del Moro, A., et al. 2014, [ApJ](#), **785**, 17
- Lansbury, G. B., Gandhi, P., Alexander, D. M., et al. 2015, [ApJ](#), **809**, 115
- Lawrence, A., Warren, S. J., Almaini, O., et al. 2007, [MNRAS](#), **379**, 1599
- Liu, Z., Merloni, A., Georgakakis, A., et al. 2016, [MNRAS](#), **459**, 1602
- Luo, B., Brandt, W. N., Xue, Y. Q., et al. 2017, [ApJS](#), **228**, 2
- Lyu, J., Rieke, G. H., & Shi, Y. 2017, [ApJ](#), **835**, 257
- MacLeod, C. L., Ross, N. P., Lawrence, A., et al. 2016, [MNRAS](#), **457**, 389
- Mainzer, A., Bauer, J., Grav, T., et al. 2011, [ApJ](#), **731**, 53
- Maiolino, R., Comastri, A., Gilli, R., et al. 2003, [MNRAS](#), **344**, L59
- Mateos, S., Alonso-Herrero, A., Carrera, F. J., et al. 2012, [MNRAS](#), **426**, 3271
- McMahon, R. G., Banerji, M., Gonzalez, E., et al. 2013, [Msngr](#), **154**, 35
- Mendez, A. J., Coil, A. L., Aird, J., et al. 2013, [ApJ](#), **770**, 40
- Menzel, M.-L., Merloni, A., Georgakakis, A., et al. 2016, [MNRAS](#), **457**, 110
- Morrissey, P., Conrow, T., Barlow, T. A., et al. 2007, [ApJS](#), **173**, 682
- Myers, A. D., Palanque-Delabrouille, N., Prakash, A., et al. 2015, [ApJS](#), **221**, 27
- Palanque-Delabrouille, N., Magneville, C., Yèche, C., et al. 2016, [A&A](#), **587**, A41
- Papovich, C., Shipley, H. V., Mehrrens, N., et al. 2016, [ApJS](#), **224**, 28
- Pâris, I., Petitjean, P., Aubourg, É., et al. 2018, [A&A](#), **613**, A51
- Pâris, I., Petitjean, P., Ross, N. P., et al. 2017, [A&A](#), **597**, A79
- Peters, C. M., Richards, G. T., Myers, A. D., et al. 2015, [ApJ](#), **811**, 95
- Pierre, M., Pacaud, F., Adami, C., et al. 2016, [A&A](#), **592**, A1
- Planck Collaboration, Ade, P. A. R., Aghanim, N., et al. 2016, [A&A](#), **594**, A13
- Pons, E., & Watson, M. G. 2014, [A&A](#), **568**, A108
- Raichoor, A., Comparat, J., Delubac, T., et al. 2017, [MNRAS](#), **471**, 3955
- Richards, G. T., Fan, X., Newberg, H. J., et al. 2002, [AJ](#), **123**, 2945
- Richards, G. T., Myers, A. D., Peters, C. M., et al. 2015, [ApJS](#), **219**, 39
- Ross, N. P., Myers, A. D., Sheldon, E. S., et al. 2012, [ApJS](#), **199**, 3
- Ruan, J. J., Anderson, S. F., Cales, S. L., et al. 2016, [ApJ](#), **826**, 188
- Runnoe, J. C., Cales, S., Ruan, J. J., et al. 2016, [MNRAS](#), **455**, 1691
- Sanders, D. B., Soifer, B. T., Elias, J. H., et al. 1988, [ApJ](#), **325**, 74
- Satyapal, S., Abel, N. P., & Secrest, N. J. 2018, [ApJ](#), **858**, 38
- Scoville, N., Aussel, H., Brusa, M., et al. 2007, [ApJS](#), **172**, 1
- Shappee, B. J., Prieto, J. L., Grupe, D., et al. 2014, [ApJ](#), **788**, 48
- Smee, S. A., Gunn, J. E., Uomoto, A., et al. 2013, [AJ](#), **146**, 32
- Smith, K. L., Koss, M., & Mushotzky, R. F. 2014, [ApJ](#), **794**, 112
- Stern, D., Eisenhardt, P., Gorjian, V., et al. 2005, [ApJ](#), **631**, 163
- Sutherland, W., & Saunders, W. 1992, [MNRAS](#), **259**, 413
- The Astropy Collaboration, Price-Whelan, A. M., SipHocz, B. M., et al. 2018, [AJ](#), **156**, 123
- Timlin, J. D., Ross, N. P., Richards, G. T., et al. 2016, [ApJS](#), **225**, 1
- Trouille, L., Barger, A. J., & Tremonti, C. 2011, [ApJ](#), **742**, 46
- Viero, M. P., Asboth, V., Roseboom, I. G., et al. 2014, [ApJS](#), **210**, 22
- Wright, E. L., Eisenhardt, P. R. M., Mainzer, A. K., et al. 2010, [AJ](#), **140**, 1868
- Xue, Y. Q., Luo, B., Brandt, W. N., et al. 2011, [ApJS](#), **195**, 10
- Yang, Q., Wu, X.-B., Fan, X., et al. 2018, [ApJ](#), **862**, 109
- York, D. G., Adelmann, J., Anderson, J. E., Jr., et al. 2000, [AJ](#), **120**, 1579